iScience

Article

Sphingolipid-neutralizing molecular therapy reduces psychosine cytotoxicity in Krabbe disease

Graphical abstract

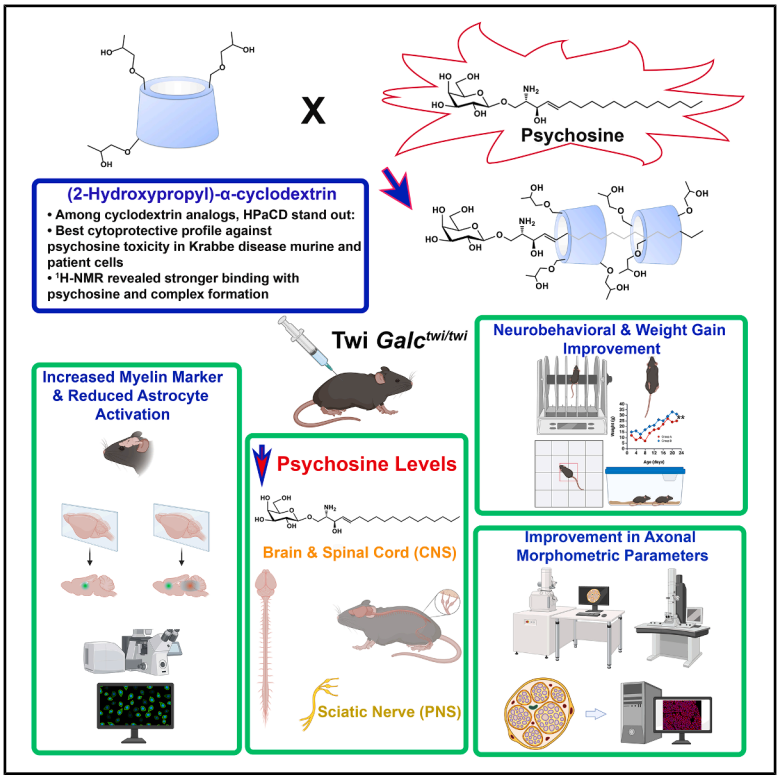

Highlights

- Krabbe disease (KD) is an inherited leukodystrophy showing high psychosine (PSY) levels
- HPaCD has a cytoprotective effect by molecularly shielding PSY
- HPaCD also facilitates the PSY clearance, reducing its levels in the CNS and PNS
- HPaCD-treated KD mice improved neurobehavior, CNS, and PNS myelin, without ototoxicity

Authors

Salma Begum, Shin-Chang Hsueh, Ezra M.Y. Cheria, ..., Michael H. Gelb, Chang-Chun Ling, Gustavo H.B. Maegawa

Correspondence

gm3025@cumc.columbia.edu

In brief

Medicine; Neurology; Pathophysiology

Begum et al., 2026, iScience *29*, 114808
March 20, 2026
https://doi.org/10.1016/j.isci.2026.114808

CellPress

iScience

CellPress
OPEN ACCESS

Article

Sphingolipid-neutralizing molecular therapy reduces psychosine cytotoxicity in Krabbe disease

Salma Begum,[1] Shin-Chang Hsueh,[1] Ezra M.Y. Cheria,[2] Jayar Espejo,[3] Ping Zhang,[3] Armand Collin,[4] Edgar Kappauf,[4] Murielle Mardenli,[4] Michael H. Gelb,[5] Chang-Chun Ling,[3] and Gustavo H.B. Maegawa[1,6,*]

[1]Department of Pediatrics (Genetics and Metabolism), Columbia University Irving Medical Center, New York, NY 10032, USA
[2]Biomarkers Core Laboratory (BCL) at the Irving Institute for Clinical and Translational Research, Columbia University Irving Medical Center, New York, NY 10032, USA
[3]Department of Chemistry, University of Calgary, Calgary, AB T2N 1N4, Canada
[4]NeuroPoly Lab, Institute of Biomedical Engineering, Polytechnique Montréal, Université de Montréal, Montréal, QC H3T 1J4, Canada
[5]Department of Chemistry, University of Washington, Seattle, WA 98195, USA
[6]Lead contact
*Correspondence: gm3025@cumc.columbia.edu
https://doi.org/10.1016/j.isci.2026.114808

SUMMARY

The deficiency of β-galactosylceramidase causes a lysosomal leukodystrophy, known as Krabbe disease (KD), resulting in elevated psychosine (PSY) levels, which are highly cytotoxic to myelin-forming cells. 2-hydroxypropyl-α-CD (HPaCD), a cyclic-oligosaccharide containing a lipophilic central cavity and hydrophilic outer surfaces, significantly reduces PSY cytotoxicity in cultured KD patient cells. Further ^{1}H-NMR studies revealed stronger interactions between HPaCD and PSY. Regarding safety, HPaCD-treated mice showed no electrophysiological and histological ototoxicity signs. In the murine KD model, HPaCD improved neurobehavior and reduced PSY levels in the CNS and PNS. The reduction of astrogliosis, increased myelin basic protein, and improvements in PNS axonal-myelin morphometrics were also observed in HPaCD-treated mice. In summary, this is an innovative therapeutic approach that leverages HPaCD's dual properties of molecularly shielding and neutralizing PSY and facilitating its CNS and PNS clearance. Since several newborn screening programs currently include KD, HPaCD becomes highly important as an adjunctive/bridge therapy for improving outcomes in this devastating disorder.

INTRODUCTION

Globoid-cell leukodystrophy, also known as Krabbe disease (KD), is a neuronopathic lysosomal disorder caused by the deficiency of lysosomal β-galactosylceramidase (Galc) secondary to biallelic pathogenic variants in the *Galc* gene. Because of the Galc deficiency, the degradation of its two primary galactosphingolipid substrates, galactosylceramide (GalCer) and psychosine (galactosylsphingosine), are found at increased levels in the nervous system.[1] The GalCer accumulation in macrophages and microglia results in the pathological hallmark of KD: multinucleated histiocytes known as globoid cells, initially described in the central nervous system (CNS).[2] Whereas psychosine (PSY) is highly toxic to myelin-forming cells, such as oligodendrocytes and Schwann cells, in the CNS and peripheral nervous system (PNS), respectively. Previous studies have shown that PSY disrupts the architecture and composition of lipid rafts and activates apoptotic pathways that ultimately lead to demyelination.[3–7] Among the clinical forms, the infantile KD is the most prevalent, known as "classic," and subdivided into early- and late-infantile, with disease onset before or after six months, respectively, and with a relatively homogenous disease progression.[8,9] More recent data indicate that the infantile KD clinical form represents ~70% of affected patients, and 30% with later disease onset from childhood to adulthood.[8,10] Slower progressive clinical forms with later disease onset of KD are less clinically characterized and systematically investigated, and may be misdiagnosed and their prevalence underestimated.[10,11] In terms of treatment, hematopoietic stem cell transplantation (HSCT) is the current mainstay therapy for delaying disease progression and extending the lifetime of patients diagnosed with early-onset forms of KD. HSCT brings the best outcomes when performed before the onset of symptoms.[12,13] In addition to being a possible source of Galc, HSCT may exert a neuroprotective effect by reducing neuroinflammation.[14,15] Despite comorbidities, HSCT slows the rate of disease progression and improves CNS pathology, while a less significant effect is observed in the PNS, possibly due to the limited cross-correction of Schwann cells.[16–18] The development of engineered adeno-associated virus (AAV) capsids capable of penetrating the blood-brain barrier (BBB) supports two AAV-based clinical trials for KD (NCT04771416 and NCT05739643/NCT06308718), which were

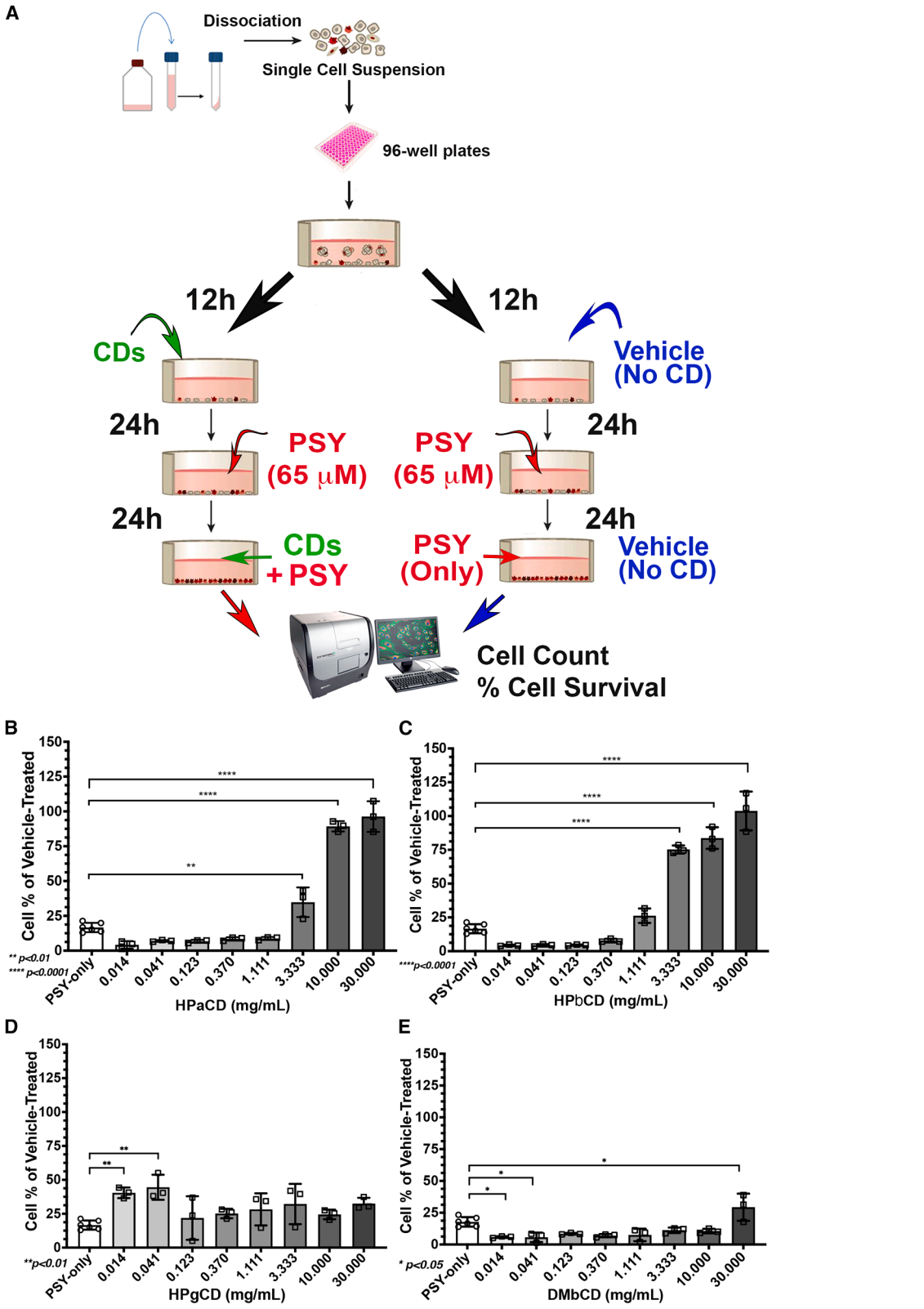

(legend on next page)

recently launched.[19] The NCT04771416 study is assessing the efficacy of *GALC* delivery into the *cisterna magna* using a modified AAV9 vector. Meanwhile, the NCT05739643 trial examines the combined effect of HSCT and *GALC* intravenously (i.v.) delivery using AAVrh10. Unfortunately, due to funding constraints, the NCT04771416 study has been suspended. The NCT05739643/NCT06308718 studies are currently active but not recruiting.

The cyclodextrins (CDs) are cyclic oligosaccharides composed of six, seven, or eight α-D-glycopyronosyl units linked by α(1->4) bonds assembled in a ring configuration, forming lipophilic central cavities and hydrophilic outer surfaces. These molecules are traditionally used as excipients and absorption enhancers for hydrophobic molecules.[20] Among different CD derivatives, 2-hydroxypropyl-β-cyclodextrin (HPbCD) has shown efficacy in Niemann-Pick Disease Type C1 (NPC1), a lysosomal neurodegenerative disorder, and is currently being evaluated in clinical trials.[21–23] During *in vivo* experiments to characterize small molecules identified in a cell-based LC-MS/MS throughput screening for psychosine-reducing molecules,[24] the *Twitcher* mice (*Twi*) receiving HPbCD-only (vehicle-control) showed a small but statistically significant extension of the *Twi* lifespan, along with the preservation of myelinated fibers in the PNS.[25] The *Twi* is a naturally occurring C57BL/6 *Galc*$^{twi/twi}$ mouse that reliably recapitulates the early-onset neurological phenotype of KD, displaying GALC deficiency due to biallelic nonsense *Galc* variants, resulting in secondary PSY elevation.[26] As previously described, HPbCD has been used as a dissolvent to solubilize highly hydrophobic candidates for murine experiments.[20] Despite not impacting the levels of PSY in the CNS and PNS, ultrastructural and morphometric studies showed statistically significant preservation of myelinated axons in the *Twi Galc*$^{twi/twi}$ mice receiving HPbCD-only. HPbCD and other CDs have been shown to cross the BBB at a slow rate via a non-saturable mechanism consistent with transcellular diffusion.[27] In addition, due to the reported effects on the lipid rafts microdomains of the BBB,[28–30] 2-hydroxypropyl-α-CD (HPaCD) has a superior permeability than HPbCD, 2-hydroxypropyl-γ-CD (HPgCD), and heptakis(2,6-di-*O*-methyl)-βCD (DMbCD).[20,31] Herein, based on the initial serendipitous observation of the impact of a CD molecule in the classical KD murine mode,[25] a series of experiments shows that HPaCD mitigates the cytotoxicity of PSY in cultured brain-derived cells, and exhibits significant interactions with PSY, as confirmed by ^{1}H-NMR. Further *in vivo* studies suggest that HPaCD functions as a neutralizing agent of PSY, improving its clearance and potentially serving as a treatment for KD. Furthermore, our findings should guide further studies on the structure-activity relationships of other CD analogs targeting PSY.

RESULTS

Screening classes of cyclodextrins with cytoprotective properties against psychosine

One of the CD analogs, HPbCD, has been shown to be efficacious in another neuronopathic lysosomal disorder, NPC1, an autosomal recessive inherited disorder caused by pathogenic variants in the *NPC1* (95%) and *NPC2* (∼5%) genes.[21,22] Using commercially available CDs, the cytoprotective effects of HPaCD, HPbCD, HPgCD, and DMbCD against PSY were examined (Figure 1). Minimal concentrations of PSY in culture media cause substantial cytotoxicity.[32] First, we selected cultured primary fibroblasts from a KD patient with the mutant *GALC*-L224P/Δ30kb variant. Second, using these cells seeded into a 96-well plate with ∼8,500 cells/well, a PSY cytotoxicity dose-response was performed. KD primary fibroblasts were exposed for 24 h with PSY concentrations ranging from 0.031 to 250 μM (Figure S1). The PSY concentration of 65 μM in the culture medium after 24 h was selected for further experiments, as it resulted in 80–85% cell death (Figure S1). Based on previous assays to examine the cytotoxicity of CD analogs, KD patient primary fibroblasts were treated with seven concentrations of each CD analog, ranging from 0.014 to 30 mg/mL, for a 24-h period. Subsequently, cells underwent a "PSY challenge" by adding PSY at 65 μM into the culture media containing the CD analogs (or vehicle, containing PBS) for another 24h period (Figure 1A). After 24h exposure to PSY, cells were washed with PBS, fixed with paraformaldehyde (PFA, 4%), and stained 4′,6-diamidino-2-phenylindole for outcome of cell counts (Figure 1A). In the same experiment, another set of wells of the 96-well plates contained cells only exposed to the vehicle of PSY, which served as a reference from which the % of remaining cells in different experimental conditions was calculated (Figure 1A). The HPaCD- and HPbCD-treated cells showed substantial cell survival at 3 to 30 mg/mL concentrations (Figures 1B and 1C). The CDs with larger molecular size cyclic rings, such as HPgCD and DMbCD, failed to show a dose-response pattern (Figures 1D and 1E).

2-hydroxypropyl-α-CD cytoprotective effects against psychosine

To confirm the cytoprotective effects of HPaCD against PSY, the calcein AM Blue (blue live-cell stain)/ethidium homodimer III (EthD-III; red dead-cell stain) cell survival assay was used to precisely ascertain the number of live and dead fibroblasts pre-treated with HPaCD, followed by the PSY challenge (Figure 2A). The non-fluorescent calcein AM permeates the intact fibroblast membrane and is converted into its fluorescent

Figure 1. KD patient cultured primary fibroblast evaluation of cyclodextrin (CD) analogs

(A) Psychosine Cellular Assay. First, primary fibroblast cells from a KD patient (*GALC*-L224P/Δ30kb) were established and seeded into 96-well plates at 8,500 cells/well. After 12h, cells were treated with different concentrations of CDs (α (a), β(b), γ(g), and DM-b-CD, ranging from 0.04 to 30 mg/mL (n = 3 wells/concentration). Vehicle-control was set as a reference ("No CD"). After 24 h of treatment, psychosine (PSY) at 65 μM was added to the culture media containing CDs at different concentrations. One set of wells (n = 6 wells) received vehicle only (no PSY) as a reference for the toxicity of CD compounds. The KD patient fibroblasts were exposed to PSY for 24 h followed by washing, fixation, and staining with 4′,6-diamidino-2-phenylindole for cell count under an automatic high-content fluorescent microscope. Under 2-hydroxypropyl-α-cyclodextrin (HPaCD) (B), and 2-hydroxypropyl-β-cyclodextrin (HPbCD) (C) treatment, significantly higher cell numbers after the PSY "challenge" were noted. The CDs with a large "ring," 2-hydroxypropyl−γ-cyclodextrin (HPgCD) (D), and heptakis(2,6-di-*O*-methyl)-βCD (DM-b-CD) (E) failed to show a dose-response pattern. Data represent mean +/- S.D.; *p<0.05, **p<0.01, ***p<0.001, ****p<0.0001.

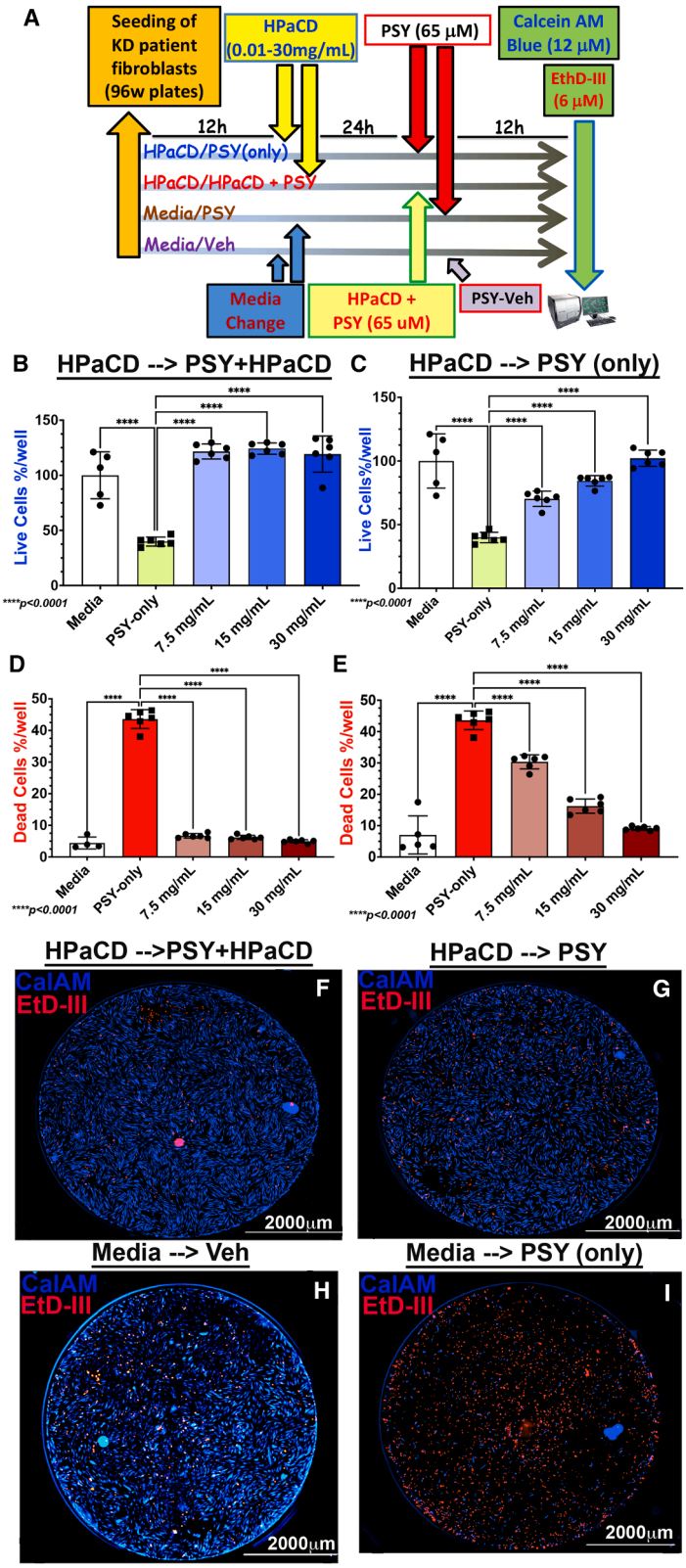

Figure 2. HPaCD-psychosine protective effects in a KD patient primary fibroblast line using CalceinAM Blue and EthD-III assay

(A) Sketch of the cellular assay timeline in which the primary fibroblast KD cell line (*GALC*-L224P/Δ30kb) was treated with a range of 2-hydroxypropyl-α-cyclodextrin (HPaCD) concentrations (0.01–30 mg/mL) and then exposed to psychosine (PSY) at 65 µM. Each line represents a set of conditions. Two conditions were examined: HPaCD/PSY, in which HPaCD was removed during the PSY challenge phase. Another condition: HPaCD/HPaCD+PSY, in which HPaCD was maintained during the exposure to PSY (65 µM). In the condition of the PSY vehicle (last line), cells were exposed to PSY and only treated with the vehicle. CalceinAM (CalAM) Blue stains live cells as it emits fluorescence (ex/em 360/445 nm) when converted to calcein by cellular esterases. Ethidium homodimer III (EthD-III) enters dead cells and binds to nucleic acids, producing red fluorescence in dead cells (ex/em 530/645 nm). Cultured fibroblasts from a KD patient (*GALC*-L224P/D30kb) were seeded in 96-well plates and pre-treated with 7.5, 15, and 30 mg/mL over 24 hs, followed by PSY challenge (65 µM). Each concentration shown represents an average of 6 wells from 96-well plates. KD patient cells were either left with HPaCD after the pre-condition treatment (B and D) or removed (C and E) before the PSY challenge. The histograms in panels B and C represent the percentage (%) of live cells/well for both HPaCD/PSY+aCD and HPaCD/PSY conditions in reference to cells exposed to media only. The histograms in panels D and E represent the percentage (%) of dead cells/well for both described conditions, compared to cells exposed to media only. Representative wells containing cells pre-conditioned with HPaCD and exposed to PSY, with the HPaCD remaining in the media (F), or removed by switching to media containing PSY only, are shown (G). Representative wells that were not preconditioned (receiving media) and exposed to vehicle (H) and PSY (I) are shown. Data represent by mean +/- S.D.; **p*<0.05, ***p*<0.01, ****p*<0.001, *****p*<0.0001.

form by intracellular esterases.[33] Thus, live primary cultured fibroblasts are indicated by the intensity of blue fluorescence in the cytosol (ex360 nm/em445 nm). EthD-III is virtually nonfluorescent and impermeant to intact fibroblastss plasma membrane. In the event of compromised cell membrane integrity associated with apoptosis, EthD-III enters cells and binds to nucleic acids, resulting in red fluorescence in dead cells (ex 530 nm/em 645 nm). In 96-well plates, HPaCD significantly increased the cell survival of KD patient fibroblasts after exposure to PSY at 65 μM (Figures 2B and 2C). Under the PSY challenge, only 20–25% of cells are detected alive (Figures 2B–2E, and 2I) compared to the vehicle control (Figures 2B–2E, and 2H). When the HPaCD remained in media during 65 μM PSY exposure, significantly higher live-cell numbers and lower dead-cell numbers were noted at concentrations from 7.5 to 30 mg/mL (Figures 2B, 2D, and 2F). In contrast, when pre-conditioning the cells by treating them with HPaCD and removing it before PSY exposure, a dose-response is observed, with the highest live-cell number and lowest dead-cell number at 30 mg/mL of HPaCD (Figures 2C, 2E, and 2G). These experiments confirmed the cytoprotective effects of HPaCD, remarkably when the cyclic molecule remained in the media pre- and during the PSY exposure (Figures 2B, 2D, and 2F).

2-hydroxypropyl-α-CD promotes intracellular clearance of psychosine

To examine whether HPaCD can reduce intracellular PSY levels, an established cell line derived from neonatal cortical brain tissue from the murine KD model (Twi *Galc*$^{twi/twi}$), developed and characterized by our group, was utilized.[24] The neuroglial Twi *Galc*$^{twi/twi}$ cell line, 145M-Twi, showed significantly higher levels of intracellular PSY in comparison to the respective control cell line 145C-WT, which is derived from C57BL6 wild-type *Galc*$^{wt/wt}$ newborn mice, as previously described.[24] Both cell lines expressed oligodendrocyte matured markers (Galc), and also glial progenitor markers (A2B5),[24] The 145M-Twi cells showed biochemical and cellular disturbances related to GLD neuropathogenesis, including remarkable caspase-3 activation, expansion of the lysosomal compartment, and increased intracellular PSY levels[24] (Figure S2A). At the same concentrations at which HPaCD showed cytoprotective properties against PSY, in a dose-response pattern, the 145M-Twi cells showed statistically significant reductions in their intracellular PSY levels after a 72-h treatment period (Figure S2B).

Cavity size-dependent stoichiometry of molecular interactions of cyclodextrins and psychosine

To investigate the potential molecular interactions of PSY with the cyclic oligosaccharides of different cavity sizes comprised of six (α), seven (β), or eight (γ) α-D-glycopyronosyl units, a ^{1}H-NMR assessment of the cytotoxic sphingolipid was performed in the presence of different CD analogs (Figure 3). The ^{1}H-NMR spectra were obtained in a potassium phosphate buffer, pH ~7, in D_2O containing 5% deuterated methanol to promote the dissolution of PSY (50 μM). The region of the spectra showing the vinyl protons of PSY is highlighted in the red box and is demonstrated in Figure 3A. The spectra of PSY alone, and PSY plus a slight excess of HPgCD (70 μM), with the largest CD cavity inner size, are virtually identical, showing no bi-molecular association (Figure 3B). In contrast, the addition of the other CDs, also at 70 μM, DMbCD, HPbCD, and HPaCD, produces detectable chemical shifts of the PSY vinyl protons (Figure 3B), indicating that they form complexes with the glycosphingolipid PSY. The vinyl proton signals in the presence of the DMbCD, HPbCD, and HPaCD are more intense than those in the sample with PSY alone or in the presence of HPgCD (Figure 3B). These findings show that PSY is not fully dissolved without binding to CD, and the binding leads to a higher concentration of PSY in the solution. Additional ^{1}H-NMR studies were carried out in the presence of a lower concentration of PSY (20 μM), which is close to the limit of detection of this lipid. The addition of 30 or 50 μM DMbCD produces identical chemical shifts of the PSY vinyl proton chemical shift values, showing that all the PSY is bound in the presence of this CD at those concentrations. These results indicate that the dissociation equilibrium constant for the complex of PSY with the three CDs is less than 20 μM. The exact values of the dissociation constants could not be obtained due to the limited detection of PSY by proton ^{1}H-NMR under these low concentrations. In summary, among the CD analogs, HPaCD, with the smallest inner hydrophobic cavity, exhibited the most pronounced chemical shift among the CD analogs tested (Figure 3B), including DMbCD and HPbCD, which have intermediate but larger cavity sizes.[20,34]

^{1}H-NMR titration of psychosine with 2-hydroxypropyl-α-CD

To further confirm the molecular interactions between PSY and HPaCD, a ^{1}H-NMR titration experiment was performed using a fixed PSY concentration (2.2 mM) and HPaCD as the titrant. The ^{1}H-NMR titration allows for the monitoring of the chemical shifts of specific protons within PSY (labeled in red letters in Figure 4A) as HPaCD (titrant) is added to the PSY solution (in D_2O) from a stock solution (6.6 mM). The ^{1}H-NMR was obtained from PSY at 17 different aliquots of HPaCD, whose concentrations ranged from 0.1 to 3.0 equivalents (Eq; Figure 4). As gradual increases of HPaCD are added to the PSY solution (2.2 mM), the peaks representing the protons of PSY are observed to increase, and those showing more significant chemical shifts are highlighted (yellow) in the titration spectra depicted in Figure 4B. While the vinyl protons H_e and H_d showed some minimal shifts with much-increased intensity (due to enhanced solubility), the protons H_b (linked to the carbon that bears the free NH_2), H_c (bound to OH^-), H_f (methylene protons next to the alkene) and the terminal H_r methyl protons showed noticeable changes in chemical shifts (Figures 4A and 4B). In addition, the remaining methylene protons H_g-H_q of the sphingosine, located throughout the long carbon chain, showed significant changes in chemical shifts, indicating the interactions with the HPaCD cavity take place mainly at the proximal aliphatic carbon chain of PSY (Figures 4A and 4B). It should be mentioned that, as the molar amount of HPaCD added to the PSY solution surpasses the 2:1 ratio, no significant changes in signals of PSY can be observed in the ^{1}H-NMR spectra (spectra 17–18). Given that the height of the HPaCD funnel measures 7.8 Å (Figure 4C), and because of the chemical shifts mapping provided by the ^{1}H-NMR titration study (Figures 4A and 4B), the proposed model

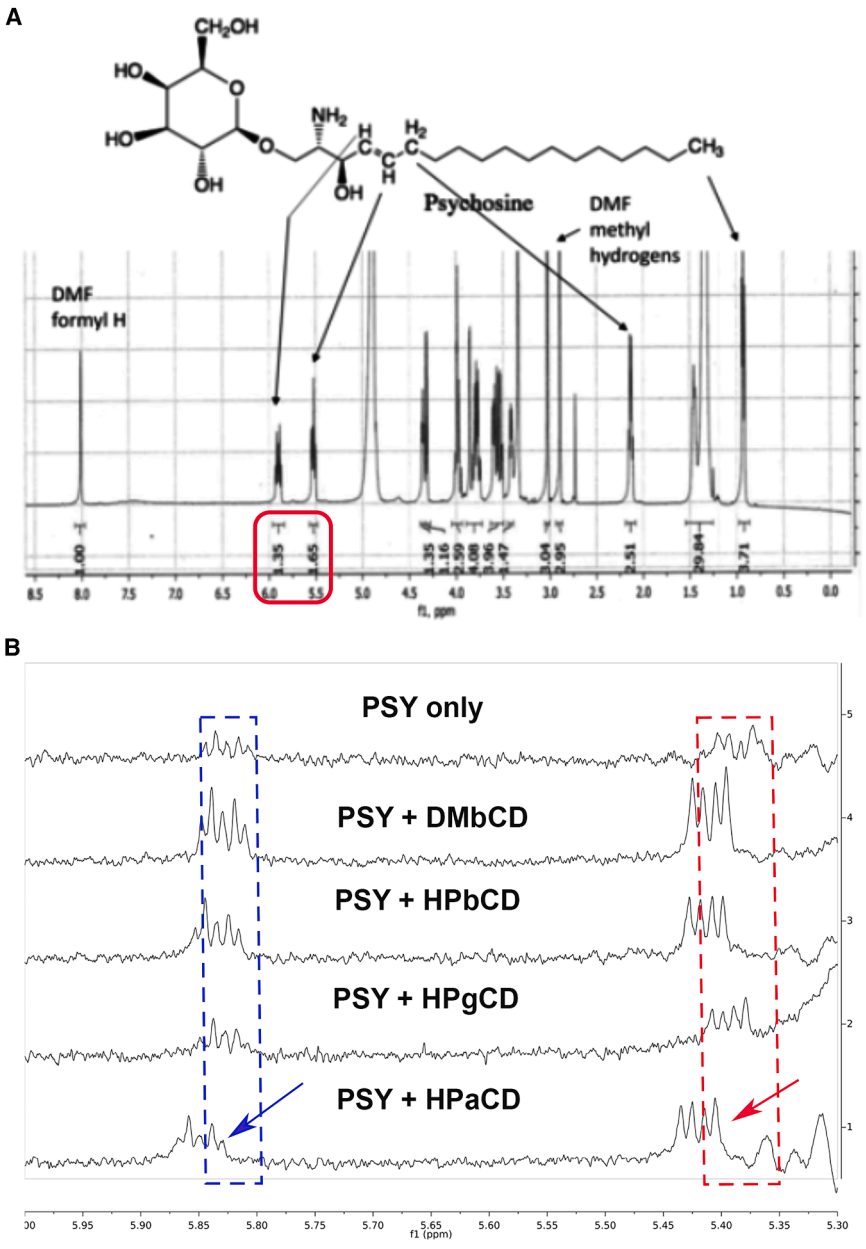

Figure 3. Proton-NMR of psychosine in the presence of cyclodextrins (CDs) derivatives

(A) Region of the proton-NMR spectra showing the two vinyl protons of psychosine at chemical shift ~5.8 ppm and ~5.4 ppm (red box).

(B) Psychosine (PSY) at 50 μM and in the presence of 70 mM cyclodextrin heptakis(2,6-di-*O*-methyl)-βCD (DM-b-CD); 70 mM 2-hydroxypropyl-β-cyclodextrin (HPbCD); 70 mM 2-hydroxypropyl-γ-cyclodextrin (HPgCD); 70 mM 2-hydroxypropyl-α-cyclodextrin (HPaCD). Significant chemical shifts of PSY were observed at 5.8 ppm (blue arrow; blue dashed box) and 5.4 ppm (red arrow; red dashed box) in the presence of HPaCD.

of the PSY: HPaCD complexation is dynamically interchanging from 1:1 to 1:2 (Figure 4D). Based on the ^{1}H-NMR cavity size-dependent stoichiometry, and HPbCD inability to reduce PSY levels in the CNS and PNS tissues *Galc*$^{twi/twi}$ murine model, as in previous reported studies,[25] HPaCD was selected for subsequent investigations.

Confirmation in Krabbe disease patient oligodendrocytes derived from human induced-neuronal stem cells

Based on the methods described earlier,[35–37] human induced-neural stem cells (hiNSCs) were established from patients with KD with specific clinical forms, including early- and late-onset KD. Leveraging the KD patient-derived iNSC cell lines established, a sufficient number of mature oligodendrocyte cells were generated. The hiNSC-derived oligodendrocytes have been shown to reliably recapitulate several pathogenic signaling pathways of neurodegenerative disorders. hiNSCs generated from primary fibroblasts of patients with KD were used to characterize small molecules in neurologically relevant KD patient-cell lines.[38] Measurements of intracellular PSY levels of the cultured hiNSC-derived oligodendrocytes (Oligos) were done by LC-MS/MS as previously described[24,39] (Figure S3). Intracellular PSY is undetectable in primary skin fibroblasts from patients with KD.[24] Therefore, the hiNSC-derived Oligos from patients with KD serve as a powerful tool for investigating the HPaCD's potential to neutralize PSY cytotoxicity. Over time, in cultured conditions, hiNSC-derived differentiated Oligos showed a significant increase in intracellular PSY levels compared with controls (Figure S3). HPaCD demonstrated robust cytoprotection in cultured iNSC-derived Oligos from patients with KD (Figures S4C and S4D). The conversion rate to mature Oligos was ~40–50%, slightly higher than in previous studies on which we based the conversion protocol.[40,41] Using immunostaining for myelin-basic protein (MBP), we determined the percentage of mature Oligos (MBP-positive cells) survival when treated with different HPaCD concentrations (Figures S4E and S4F). Interestingly, the KD patient iNSC-derived Oligos, characterized by higher levels of mature Oligo markers (Figures S4A and S4B), were highly sensitive to PSY cytotoxicity, with 1 μM sufficient to cause ~50% cell death (Figure S4C). For this reason, HPaCD concentrations ranging from 3.3 to 30 μg/mL showed a dose-dependent reduction in cell death upon exposure to PSY (1 μM; Figure S4).

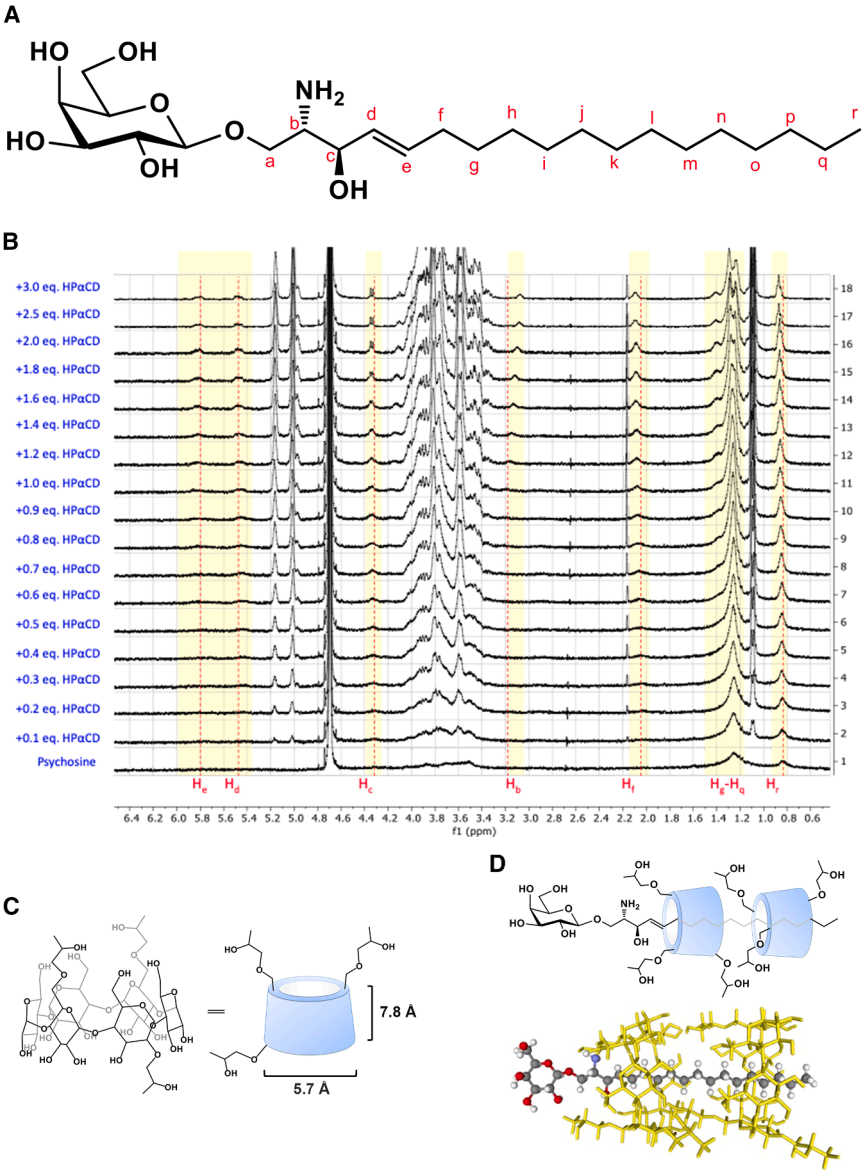

Figure 4. ^{1}H-NMR titration of psychosine in the presence of 2-hydroxypropyl– α-cyclodextrin (HPaCD)

(A) Psychosine (PSY) molecular structure with carbons labeled in red letters.

(B) ^{1}H-NMR titration spectra from an experiment with PSY (1.0 mg, 2.2 mmol) in D_2O (1.0 mL) exposed to various HPaCD concentrations ranging from 0 to 3 Equiv.(eq), resulting in the corresponding ^{1}H-NMR spectra from 1 (0 eq HPaCD), 2–11 (0.1 eq HPaCD per aliquot), 12–16 (0.2 eq HPaCD per aliquot) to 17–18 (5 eq HPaCD per aliquot) – numbers stated in the right side of panel B. The protons are indicated in "H," just below the spectra and above the f1 (ppm) axis, with red letters referring to the corresponding carbon of the PSY structure (A). The yellow-highlighted peaks are the sphingosine protons (Hc-Hr) of PSY that undergo gradual shifts upon the addition of an increasing amount of HPaCD. No significant changes were observed after a total of ∼2.0 eq of HPaCD were added to the solution.

(C) The molecular structure of HPaCD was used in the study with an average degree of substitutions (DS: ∼3.6).

(D) Proposed 1:2 inclusion model between PSY and HPαCD; the formation of PSY/HPaCD inclusion complexes is dynamically interchanging between 1:1 and 1:2.

(E) A docked model of 1:2 PSY/HPaCD inclusion complex.

Plasma, metabolic stability, and central nervous system biodistribution

As in other neurological disorders, drug candidates for KD must cross the BBB to achieve CNS penetration and ensure efficacy. Recent studies showed that CDs cross the BBB in small amounts via a non-saturable mechanism, with variable uptake among different CNS regions, which is attenuated by a brain-to-blood efflux system.[20,27,31] To assess the potential of HPaCD in generating adequate CNS biodistribution, FITC-labeled αCD (named PZ11081) was synthesized, as depicted in the synthesis route in Figure S5. Quality-control analysis of FITC-labeled αCD was performed (Figures S6A–S6C), demonstrating the prevalence of dianion isoform (i.e., structure 5'; Figure S6A). The *in vivo* studies with FITC-labeled αCD were conducted in the murine KD model, Twi *Galc*$^{twi/twi}$. Because immediate bioavailability is necessary to determine the intrinsic properties of HPaCD in achieving the CNS,[42–44] the intravenous route was chosen for the CNS biodistribution assessment. A 50 mg/kg dose of the FITC-labeled αCD was administered intravenously (IV) for the six mice assessed at each time point. A peak was noted at 1 h, and sustained levels were observed after 4 h (Figure S6D). After the last time point at 24h post-IV injection, mice were euthanized, and whole-body perfused with heparinized saline (NaCl 0.9% with 10,000 IU/L of heparin). In post-perfused brain specimens, FITC-labeled αCD measurements were consistent with plasma levels (Figure S6D), and sustained CNS drug concentrations were observed 4 h after IV administration (Figure S6E).

Effects of 2-hydroxypropyl-α-cyclodextrins in the central nervous system and peripheral nervous system

Based on previous *in vivo* studies on another CD,[45–48] the estimated dosing and *in vivo* efficacy of HPaCD in the Twi *Galc*$^{twi/twi}$ were evaluated. A cohort of fifteen Twi mice was treated at 5,000 mg/kg intraperitoneal (IP) injections daily from postnatal days (PNDs) 2–3 of life until PNDs 36–38. The IP route for the *in vivo* experiments was chosen primarily due to its ability to achieve rapid absorption and widespread distribution, similar to the IV route, and its suitability for

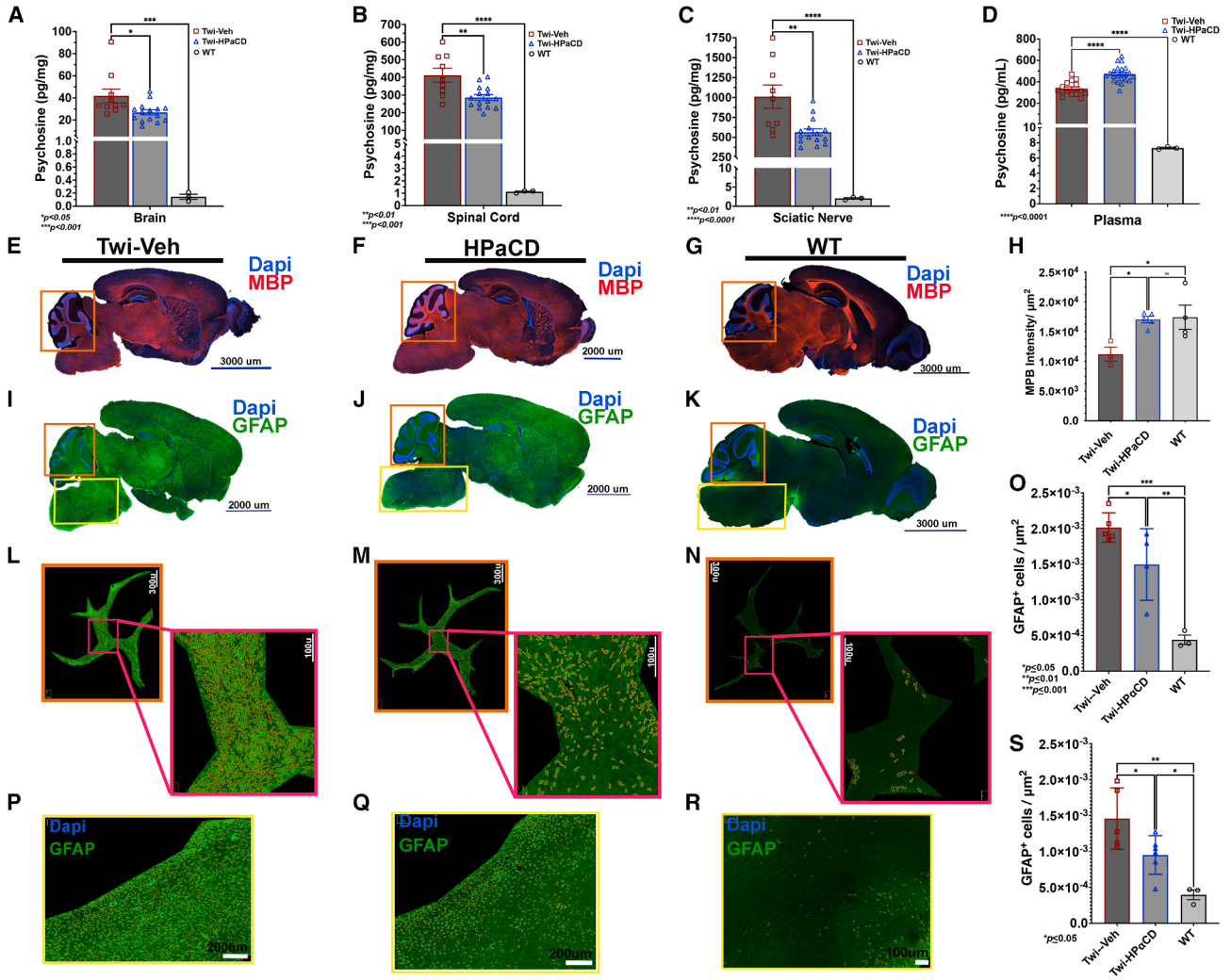

Figure 5. Effects of the HPaCD on the CNS and PNS psychosine levels, brain myelin markers, and astrocyte

Since postnatal day (PND) 2, a group of Twi *Galc*$^{twi/twi}$ (Twi) mice were treated with 5,000 mg/kg of 2-hydroxypropyl-a-cyclodextrin (HPaCD) intraperitoneal (IP) daily injections. The HPaCD-treated cohort showed a significant reduction of the psychosine (PSY) levels in brain (A), spinal cord (B), and sciatic nerve (C) specimens in comparison to those of Twi mice receiving vehicle (Twi-veh) only. PSY levels were normalized for the dry weight of the lipid extraction specimen and the total body weight of each mouse.

(D–F) Immunohistochemistry for myelin-basic protein (MBP) showed increased protein levels in white matter regions, particularly cerebellum *arboe vitae* (orange square) in brain sagittal sections of HPaCD-treated Twi mice compared to the Twi-veh cohort.

(G–I) Using a specific antibody for Glial Fibrillary Acidic Protein (GFAP) to identify astrocytes, reduction of the number and density of astrocytes was observed in the HPaCD-treated Twi (G) in comparison to the Veh-treated cohort (H), especially in the hindbrain (yellow squares) and *arbor vitae* of the cerebellum (orange squares). Yellow squares indicate the hindbrain regions, and orange squares indicate the cerebellum regions of the depicted brain sagittal sections. The age-matched WT mice showed few GFAP-positive cells throughout the brain (I). Higher magnification images of the *arbor vitae* are shown in panels and respective subpanels: L (Veh-treated Twi mouse), M (HPaCD-treated Twi mouse), and N (WT control). Higher magnification images of the hindbrain are shown in panels P (Veh-treated Twi mouse), Q (HPaCD-treated Twi mouse), and R (WT control). Quantification of astrocytes (GFAP-positive cells) in the *arbor vitae* (O) and hindbrain (S) from HPaCD-treated and veh-treated groups. Brain sagittal sections from each group were analyzed. Fifteen mice (7M;8F) were treated with HPaCD, and twelve (6M; 6F) were included in the vehicle group. Three wild-type mice (WT) were placed as control references. Data represent mean +/- S.E.M; **p*<0.05, ***p*<0.01, ****p*<0.001, *****p*<0.0001.

chronic and repeated administrations.[49] Another cohort of ten Twi *Galc*$^{twi/twi}$ mice received only the vehicle (phosphate-buffered saline, PBS) used to dissolve HPaCD. After treatment, mice were perfused, and their brains were dissected for lipid extractions for PSY measurements by LC/MS/MS, and immunohistochemistry assays were then performed. The HPaCD-treated Twi *Galc*$^{twi/twi}$ mice showed statistically significant decreases in PSY levels in both CNS (brain and spinal cord; Figures 5A and 5B) and PNS, represented by the sciatic nerves (Figure 5C). PSY levels from the identical specimens harvested from WT controls, perfused and euthanized at PND 36–38, are also shown for reference

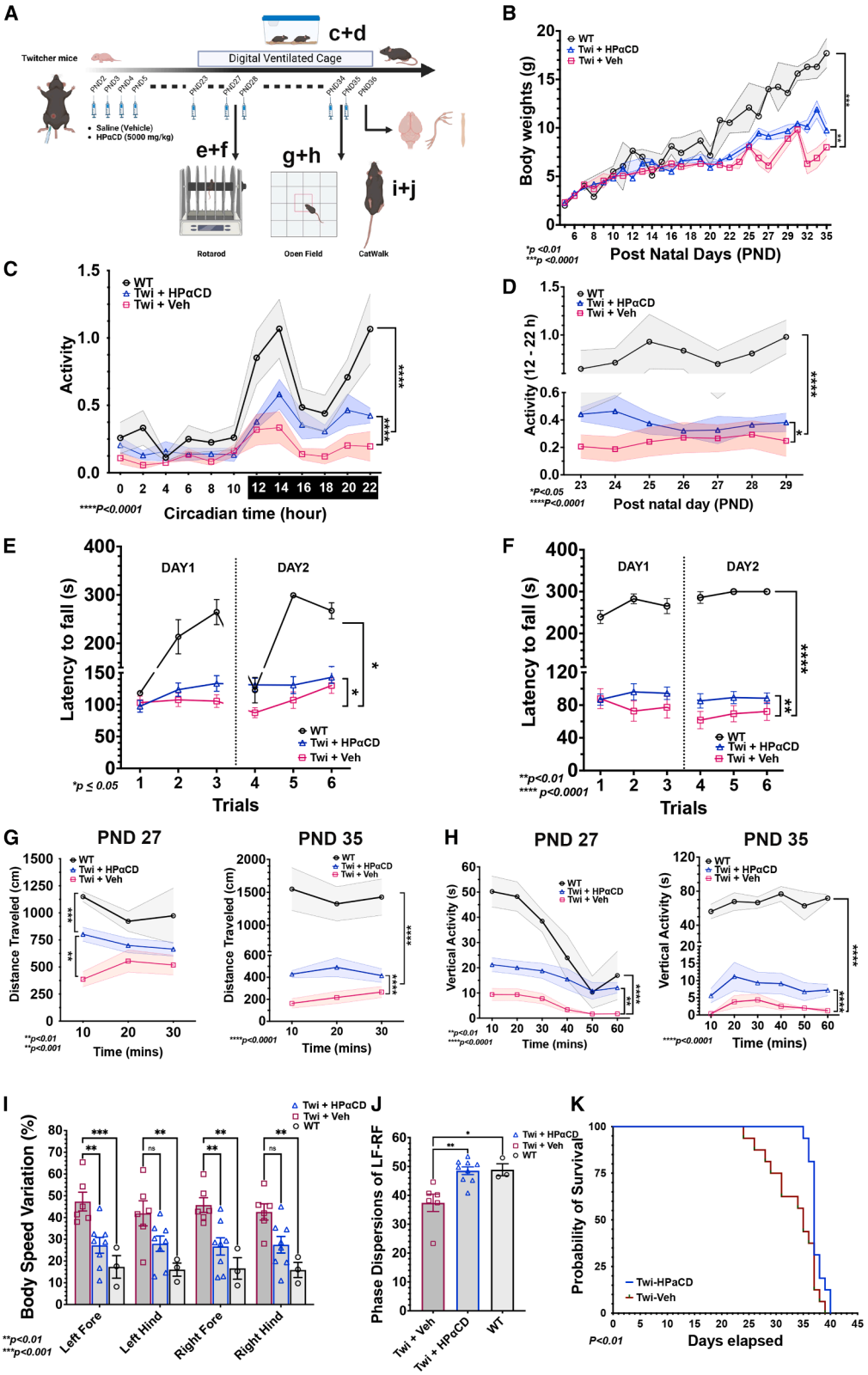

(legend on next page)

(Figures 5A–5C). Interestingly, concomitant with the reductions of PSY levels in the CNS and PNS recorded with the HPCaCD treatment, statistically significant elevations of PSY levels in the plasma of the HPaCD-treated mice were also noted (Figure 5D). Correspondent improvements in CNS myelin preservation with increased MBP levels in several areas of myelin, including the *arbor vitae* (cerebellum) in the HPaCD-treated group (Figures 5F and 5H), when compared to vehicle-treated (Figures 5E and 5H). Reductions of the astrogliosis were observed in several white matter areas, most significantly in the hindbrain (Figures 5J, 5Q) and *arbor vitae* (Figures 5J and 5M) of the HPaCD-treated compared to vehicle-control mice (hindbrain: Figures 5I and 5P; *arbor vitae*; Figures 5I and 5L). Brains from the WT control group are shown as a reference (Figures 5G, 5K, 5N, and 5R). In the specific cell-counting analysis, HPaCD showed a significant decrease in astrocytes (GFAP-positive cells) in the hindbrain (Figure 5O) and the cerebellar *arbor vitae* areas of the Twi brain (Figure 5S).

Assessment of the potential ototoxicity of 2-hydroxypropyl-α-cyclodextrins

Given the risk of ototoxicity inherent to CD molecules, we examined a cohort of 8-week-old C57BL6/J *Galc*$^{wt/wt}$ mice, the same background as the Twi mice. Eight mice (4 males and 4 females) received HPaCD at 5,000 mg/kg SC daily, and eight (4 males and 4 females) received vehicle (PBS). After 2 weeks, mice underwent acoustic startle and prepulse inhibition evaluations, whose amplitude responses (mV) showed no statistically significant differences between the HPaCD- and vehicle-treated groups (Figure S7A). After euthanasia and whole-body perfusion, each HPaCD-treated and age-matched control had the cochlear neurosensory epithelium (organ of Corti) dissected for immunohistochemistry assays to assess the integrity of the inner ear structures, as previously described.[50] The preservation of the single row of inner hair cells (IHCs) and, more importantly, the three layers of outer hair cells (OHCs) was observed in the HPaCD-treated mice group (Figure S7B). The SOX2-stained-positive supporting cells (SC) were intact in the HPaCD-treated group (Figure S7C). No statistically significant differences were noted in the Myo7a- and Sox2-stained-positive cells counted in a 200 μm area of the cochlear neurosensory epithelium (Figure S7D). Notwithstanding these findings, the HPbCD counterpart molecule traditionally causes severe hearing loss, selectively causing loss of the OHCs after a week of drug treatment, as previously described.[51–53]

2-Hydroxypropyl-α-cyclodextrins promotes clearance of psychosine in the Twi murine model

To examine the fate of neutralized PSY by HPaCD, we measured PSY levels in urine and plasma samples from Twi mice treated with 5,000 mg IP injections daily from PND 30 to 37, 7 days. The urinary concentrations of PSY showed significant increases in urine specimens collected post-7 days of HPaCD treatment (Figure S8A). Correspondingly, Twi mice showed significant enhancements in urinary clearance of PSY (Figure S8B) under HPaCD treatment. In addition, the PSY concentration in the stools of the Twi mice declined significantly with HPaCD treatment to levels not significantly different from the respective controls (Figure S8C; $p = 0.9391$).

Impact of 2-hydroxypropyl-α-cyclodextrins on body weight gain of the Twi murine model

Body weight was measured three times a week for the WT, Twi HPaCD-treated, and Twi vehicle-treated mouse groups starting at PND2 (Figure 6A). Mouse groups included an equal proportion of males and females. The Twi HPaCD-treated cohort of mice showed a significantly higher weight gain than the vehicle-treated groups ($p < 0.01$; Figure 6B).

Neurobehavioral and survival impact of 2-hydroxypropyl-α-cyclodextrins

Several neurobehavioral assessments were performed to examine the efficacy of HPaCD in ameliorating the Twi neurobehavioral phenotype, including the rotarod, open-field, CatWalk, and Digital Ventilated Cage (DVC). In the study design, mice received 5,000 mg/kg of daily IP injections from PND 2 until being euthanized at PND 35. The video-tracking of individual mice was performed in this study to establish endpoints sensitive to differences between the vehicle groups (Figure 6A). The Twi (*Galc*$^{twi/twi}$) treated with HPaCD showed statistically significant improvement in different neurobehavioral assessment tools performed blindly in the mice cohorts (Figure 6). The DVC examinations showed a statistically significant difference in the activity levels of the Twi mice, mainly at the circadian period of 12-22h (Figure 6C), consistent with the circadian activity of the murine

Figure 6. Neurobehavioral Assessments Improvements with 2-hydroxypropyl-α-cyclodextrin (HPaCD)

(A) *In vivo* study was designed to investigate the neurobehavioral effects of HPaCD in Twi *Galc*$^{twi/twi}$. Mice were administered 5,000 mg/kg intraperitoneal daily until being euthanized at postnatal day (PND) 36, when they were euthanized for harvesting specimens of the brain, spinal cord, and sciatic nerves.

(B) Mice's weights were recorded every two days during the trial, and significant differences were noted between HPaCD-treated and vehicle-treated groups. Mice were placed in the digital ventilated cage (DVC) to assess mouse activity from PND 23–29.

(C) At the initial assessment of PND 22, significant differences in mouse activity levels were noted from 12:000 to 22:00 h due to typically increased nocturnal activities. Therefore, mouse activity evaluation by DVC was performed during the selected period between PND 23–29, and activity is depicted in panel D. At PND 27 and PND 35, mice underwent the rotarod (E and F), and open-field (G and H). For the rotarod, 3 trials were performed in PND 27 & 28 (E), and PND 35 & 36 (F). For the CatWalk, the Twi was only assessed at PND27, with measurements of body speed variation (I) and distance traveled (J). Survival analysis (K) was performed in a separate Twi-HPaCD- and veh-treated mice. For the body weight, 13 mice from each group were analyzed. For the mice activity (DVC), WT ($n = 4$); Twi+HPaCD ($n = 5$); Twi+Veh ($n = 5$) were analyzed. For the rotarod, WT ($n = 3$), Twi+HPaCD ($n = 12$ for PND 27; $n = 6$, PND35), Twi+Veh ($n = 12$ at PND27; $n = 13$ at PND13) were analzyed. Fifteen mice (7M;8F) were treated with HPaCD, and twelve (6M; 6F) were included in the vehicle group. Twelve wild-type mice (WT; 6M; 6F) were followed as control references during each assessment. For the survival analysis, $n = 16$/group (8M; 8F) were used. Survival analysis was performed using the log rank (Mantel-Cox) and Gehan-Breslow-Wilcoxon tests, with p-values of 0.0081 and 0.0044, respectively. Data represent mean +/- S.E.M.; $^{*}p<0.05$, $^{**}p<0.01$, $^{***}p<0.001$, $^{****}p<0.0001$.

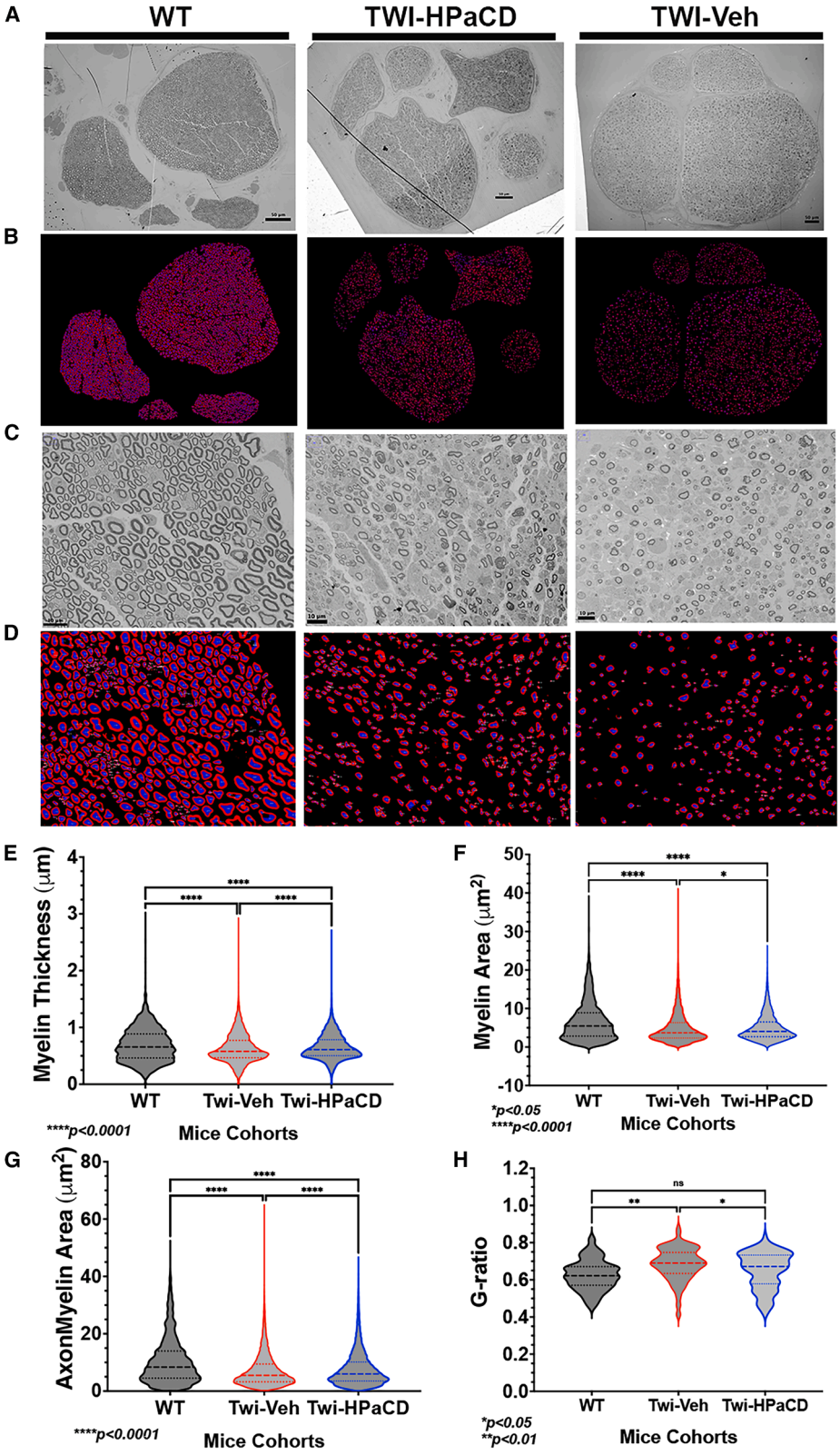

(legend on next page)

species.[54,55] This period was then selected to monitor the mice in DVC cages between PND 23 and 29. The Twi-HPaCD-treated cohort showed significantly higher activity measurements in DVC cages than the vehicle-treated cohort (Figure 6D). In the rotarod evaluations, the mice cohort receiving HPaCD showed significantly longer latency to fall time in comparison with the cohort receiving vehicle-only at PND 27 (Figure 6E) and 35 (Figure 6F) time points. In the open field assessment, the HPaCD-treated mice had significantly longer horizontal travel distances, measured at both time points (PND 27 and 35; Figure 6G). In addition, the HPaCD-treated mice demonstrated significantly higher vertical activity than the vehicle-treated group at PND 27 and PND 35 (Figure 6H). In the CatWalk XT assessments, the body speed variation, which represents fluctuations in mouse walking speed depending on each limb,[56,57] was chosen as a demyelinating disorder, significant differences were expected and observed from Twi in comparison to the age-matched WT mice (Figure 6I). The HPaCD-treated cohort showed significantly lower body speed variations at both right and left forelimbs compared to the vehicle-treated cohort (Figure 6I). The phase dispersion parameter of the CatWalk XT analysis was also evaluated as a significant phase dispersion measure suggests poor coordination – relevant to the murine model - between the compared paws.[56,57] Twi mice receiving HPaCD had significantly higher phase dispersions, more similar to the WT controls, indicating better gait coordination (Figure 6J). In a separate Twi mouse cohort, survival analysis revealed that HPaCD increased Twi mouse lifespan by a slight but significant number of days (Figure 6K).

2-Hydroxypropyl-α-cyclodextrins effects on the peripheral nervous system

Given the positive neurobehavioral effects of HPaCD, the PNS was also examined by harvesting sciatic nerves from Twi HPaCD-treated (n = 6; 3 males and 3 females), Twi vehicle-treated (n = 6; 3 males and 3 females), and WT (n = 4; 2 males and 2 females) mice groups at PND 35–36. The specimens were imaged using transmission electron microscopy (TEM), followed by axonal morphometric analysis (Figures 7A and 7C), which was performed using a deep-learning model for automated segmentation and histomorphometry of myelinated peripheral nerve fibers known as AxonDeepSeg (Figures 7B and 7C).[58] In ultrastructural studies of the sciatic nerve, as previously reported,[59] Twi mice exhibited a decreased density of axonal myelinated fibers compared to WT nerves (Figure 7A and Table S1). HPaCD partially rescued the decreased myelin thickness observed in the axons of Twi mice, as determined by measurements (Figure 7E and Table S1). The mean myelin thickness was 0.6865 ± 0.0042 mm (mean ± S.E.) in the WT cohort and 0.6297 ± 0.0019 mm (mean ± S.E.) in the TWI-Veh cohort (Table S1; $p < 0.0001$). The Twi-HPaCD cohort showed statistically significant thicker myelin than the Twi-Veh group (Figure 7E and Table S1; $p < 0.0001$). The myelin area was also significantly higher in the WT cohort, showing 6.5920 ± 0.0727 mm^2 (mean ± S.E.) in comparison to the Twi-Veh, measuring 4.8790 ± 0.0287 mm^2 (mean ± S.E.; Figure 7F and Table S1; $p < 0.0001$). Meanwhile, when treating the Twi with HPaCD, significant increases in myelin area were observed ($p < 0.05$; Figure 7F and Table S1). In addition, the HPaCD treatment significantly increased the axon-myelin area, which measured 7.680 ± 0.047 mm^2 (mean ± S.E.) in the Twi-HPaCD group and 7.214 ± 0.044 mm^2 in the Veh-treated group (mean ± S.E.; Figure 7G and Table S1; $p < 0.0001$). As previously described,[15,60] the G-ratio was significantly increased in the vehicle-treated Twi mice cohort at 0.6841 ± 0.0080 (mean ± S.E), in comparison to the WT mice cohort at 0.6256 ± 0.0129 (mean ± S.E.; Figure 7H and Table S1; $p < 0.01$). The HPaCD treatment significantly reduced the g-ratio in the Twi mice to 0.6500 ± 0.0090 (mean ± S.E.; $p < 0.05$), making it non-statistically different from the WT G-ratio (Figure 7H and Table S1). Other specific axonal morphometric measurements, including axonal diameter (Figure S9A), axonal perimeter (Figure S9B), and axon-myelin perimeter (Figure S9C), showed significant increases in HPaCD-treated animals. Interestingly, axonal density did not differ significantly between the HPaCD-treated and vehicle-treated groups (Figure S9D). In summary, the data indicate that HPaCD treatment enhances several ultrastructural morphometric parameters of the sciatic nerves in the KD murine model. HPaCD also showed evidence of improving the neuroinflammatory component in the PNS, as shown by reducing the number of multinucleated cells (KD globoid-cells) and macrophages along with TNFα levels in the sciatic nerves of the TWI-treated mice (Figure S10).

DISCUSSION

Globoid-cell leukodystrophy, known as KD, is a progressive lysosomal leukodystrophy with limited disease-modifying treatment options, particularly for patients who are already symptomatic or have late-onset KD. The current standard therapy with hematopoietic stem cell therapy (HSCT), which provides for Galc cross-correction and reduction of neuroinflammation, has

Figure 7. Effects of the 2-hydroxypropyl-α-cyclodextrin (HPaCD) in the peripheral nervous system examined by an automated deep-learning morphometrics model of axonal ultrastructural TEM images

(A) Representative ultra-structure transmission electron microscopy (TEM) of sciatic nerves of PND 35 mice wild-type C57BL6 (WT) and Twitcher (Twi-HPaCD, which were treated with 2-hydroxypropyl-α-cyclodextrin (HPaCD) or Twi-Vehicle (Twi-Veh), which received only saline. The first row shows lower-magnification TEM images of representative sciatic nerve bundle cross-sections.

(B) Automated axon/myelin segmentation of the cross-section is shown in A.

(C) Higher magnification of the region of interest from A.

(D) Higher magnification of the automated axon/myelin segmentation of the cross-section of panels A and B. Violin boxplot shows the following axon morphometrics measurements, including myelin thickness (E), myelin area (F), axon-myelin area (G), and G-ratio (H) from the three mouse cohorts: WT, TWI-HPaCD, and TWI-Veh. Data represent mean ± S.E.M. (*$p < 0.05$, **$p < 0.01$, ***$p < 0.001$, ****$p < 0.0001$) of $n = 4$ control WT mice, $n = 6$ HPaCD-treated, and $n = 6$ TWI Veh-treated. *ns*, not significant. The number of axons analyzed for each axonal morphometric parameter is as follows: wild-type (WT): 4,628; Twi-Veh: 24,192; Twi-HPaCD: 25,371. Scale bars, 10 μm and 50 μm.

inherent co-morbidities and efficacy that is mainly restricted to asymptomatic children with early onset clinical forms of KD.[12,13,61,62] Recently, the combination of HSCT with AAV-mediated gene therapy has been shown to have synergistic effects in animal models of KD,[63] and is currently under long-term follow-up in a clinical trial (NCT04693598).

Cyclodextrins (CDs) are cyclic oligosaccharides with α-(1,4)-linked D-glucopyranosyl units. The degree of polymerization is designated by Greek letters α, β, and γ, which designate cyclodextrins containing 6, 7, and 8 glucose units, respectively. CDs were the first organic compounds found to form complexes with other organic molecules, as described by Cramer (1954).[64] The complexing ability of CDs results from the spatial arrangement of glucose moieties: the hydrophilic primary and secondary hydroxyl groups are located on the outer side of the circular, torus-shaped molecule, thereby rendering the inner side of the torus more lipophilic.[34] Hence, small lipophilic molecules that fit in this ring as a "host," may form an inclusion complex (Figures 4C and 4D). However, the forces that stabilize these complexes are relatively weak, and the dissociation of the complex usually occurs readily, even by adding an excess of water.[34]

Several CDs have been used therapeutically. Among the lysosomal diseases, HPbCD has shown efficacy in Niemann-Pick Disease Type C1 (NPC1), an inborn lysosomal disorder, and is currently being evaluated in clinical trials.[21–23] HPbCD mobilizes stored cholesterol in NPC1-deficient cells, improves neurobehavioral function, and extends the lifespan of *Npc1*$^{-/-}$ mice.[21–23] Interestingly, more recently, HPbCD was shown to rescue the loss of OLIG2-positive cells in the corpus callosum of *Npc1*$^{-/-}$ mice, suggesting concomitant improvement in oligodendrocyte cell lineage survival, maturation, and myelination, which is guided by an epigenetic cascade process.[23]

Based on an initial serendipitous observation,[25] a series of cellular and ^{1}H-NMR experiments (Figures 3 and 4) showed that the cavity size-dependent stoichiometry of the CD-PSY complex impacts their cytoprotective effects (Figures 1 and 2). In previous work, HPbCD demonstrated statistically significant extension of survival and preservation of myelinated axonal fibers in the Twi mouse.[25] Further examination of other CDs showed that HPaCD, a cyclic-oligosaccharide assembled in a six-sugar ring configuration containing smaller lipophilic central cavities and hydrophilic outer surfaces, significantly prevents the cytotoxicity of the PSY in cultured KD patient-derived primary fibroblasts (Figure 2). In addition, in subsequent studies, clearance of the endogenous PSY observed in the neuroglial Twi mouse-derived cells (145M-Twi)[24] was observed (Figure S2). Even after removing the compound from the culture media, significant protection against PSY cytotoxicity was observed in a dose-response manner (Figures 2C and 2E). To further evaluate the impact on human neurologically relevant cells, using the CalAM/EtD-III assay, iNSC-derived Oligos from a KD patient showed significantly higher live-cell numbers (Figure S4).

Interestingly, mature iNSC-derived Oligos from patients with KD were more susceptible to PSY toxicity, and 1 μM was sufficient to cause ∼50% cell death (Figure S4C). Therefore, the HPaCD concentrations of 3.3–30 μg/mL resulted in dose-response toxicity when KD patient hiNSC-derived Oligo was exposed to 1 μM (Figure S4). In summary, the reported results indicate that HPaCD promotes cytoprotection against PSY first in primary KD fibroblasts (Figure 1) and, subsequently, in iNSC-derived Oligos. This phenomenon is attributed to the neutralizing effects of HPaCD, which forms a complex with PSY (Figure 4). In addition, HPaCD carries dual properties in both neutralizing/shielding PSY (Figures 1, 2, and S4C) and promoting its clearance (Figure S2), which can occur synergistically. This synergistic, rather than additive, effect of HPaCD may explain the nearly complete rescue of live cells at higher HPaCD concentrations. In addition, HPaCD may enhance the clearance of secondary sphingolipids, thereby improving lysosomal function in the setting of Galc deficiency in KD.

To investigate the molecular mechanism of action, further ^{1}H-NMR studies with different cavity-size CDs showed the most noticeable chemical shifts with the HPaCD molecule (Figures 3 and 4), indicating that HPaCD with six α-D-glucopyranosyl units binds strongly and sequesters PSY, neutralizing its cytotoxicity effects as observed in prior cellular experiments (Figures 1, 2, and S4). Notably, the chemical shifts of vinyl proton signals (∼5.8 and ∼5.4 ppm) produced by HPbCD and DMbCD indicate a stoichiometric molecular interaction with PSY. Importantly, among the CD analogs, DMbCD has the highest cholesterol affinity, binding, and extraction capacities.[65] Given these properties, in a cell culture environment, PSY molecules compete with abundant cholesterol molecules residing in cell membranes for binding to the inner hydrophobic cavity. The latter complexation can cause further cell cytotoxicity due to the extraction of membrane cholesterol.[65] Thus, DMbCD high-cholesterol extraction capacity can result in the lack of a cytoprotective dose-response of this CD analog, as observed in early PSY challenge cell experiments (Figure 1). Whereas HPbCD, with a superior chemical shift for both PSY vinyl protons in comparison to DMbCD (Figure 4B), shows evidence of better binding with PSY, though inferior to HPaCD, whose chemical shifts were the most pronounced among the CDs examined. Based on the ^{1}H-NMR spectra of PSY, HPaCD also showed prominent interactions taking place with the methylene protons of the hydrophobic aliphatic chain (Figure 4B). Since HPaCD is a six α-D-glucopyranoside cyclic oligomer with an internal diameter of 0.56 nm (Figure 4C), it is conceivable that PSY, a glycosylsphingoid consisting of sphingosine having a β-D-galactosyl residue attached at the 1-position, will interact with the straight chain region to form complexes. Interestingly, when attentively observing the ^{1}H-NMR titration spectra in Figure 4B, both the protons proximal to the galactose head group, such as H_b, (NH_2-bound), H_c (OH-bound), H_e, and H_d (vinyl protons), and the terminal carbon (H_r) generated smaller but noticeable changes in chemical shifts (Figures 4A and 4B). In addition, the C18 length of the sphingosine tail measures ∼27.7 Å[66] and the "height" of the HPaCD is 7.8 Å[34] (Figure 4C). Taken together, these observations indicate and favor the 2:1 dynamic complexation of HPaCD:PSY as depicted in Figure 4D.

Based on the ^{1}H-NMR results, a fluorescently labeled HPaCD was synthesized to allow the determination of CNS biodistribution (Figure S5). Given the challenges and level of complexity CDs can form with different lipids,[34] similar approaches using fluorescently labeled CDs to study pharmacokinetic properties have been previously performed.[67] The

mono-FITC-labeled αCD, FITCαCD, existing in equilibrium between the open and spirocyclized forms (Figure S6A), showed a significant degree of purity by high-resolution mass spectrum at $^{+}$ESI (Figures S6B and S6C). In the drug *in vivo* assessment, FITC-αCD showed stable levels both in plasma and in CNS after the initial peak after single-dose IV administration (Figures S6D and S6E). The results are consistent with previous studies demonstrating increased CNS bioavailability, particularly for αCDs.[20] Although the brain CNS levels are considered low (Figure S6E), it is important to note that the dose injected (50 mg/kg) is 100-fold lower than that used in subsequent studies (5,000 mg/kg). Thus, based on the latter dose of HPaCD used in subsequent studies, the CNS drug levels are expected to be higher than those achieved with the FITC-labeled αCD parent compound.

From our and others' published studies, no detection and differences in intracellular PSY levels are observed between the KD patient primary fibroblasts (such as the Galc-L224P/Δ30kb line) and healthy controls.[24,32] For this reason, we developed the PSY challenge assay by determining the critical PSY concentration (∼80uM) in the cultured media, after which only ∼20–35% of cells survive in cultured primary fibroblasts (Figure S1). In addition, a neuroglial line was established from brain cortices harvested from neonatal murine *Galc*$^{twi/twi}$ pups, named the 145M-Twi cell line, which was previously described and characterized.[24] The 145M-Twi cell line shows significantly elevated endogenous PSY levels compared to the corresponding control, 145C-WT (Figure S2A). Thus, the 145M-Twi cells proved to be a robust immortalized cell line for examining intracellular PSY clearance in the presence of HPaCD, as shown in Figure S2B. The HPaCD functions both as a neutralizing agent (Figures 1 and 2) and as a promoter of psychosine clearance (Figure S2B). Further along, in the *in vivo* experiments, the Twi murine model shows increased urinary clearance of PSY after HPaCD treatment (Figure S8). HPaCD was shown to impact the PSY levels in the CNS and PNS, significantly reducing its levels in the brain, spinal cord, and sciatic nerves from HPaCD-treated Twi mice (Figures 5A–5C). As per immunohistochemistry assays, HPaCD significantly increased MBP (Figures 5F and 5H) and reduced astrocyte density in several brain regions (Figures 5J, 5Q, 5M, 5O and 5S). In addition, reductions in the numbers of multinucleated and macrophage cells were observed in sciatic nerve specimens from HPaCD-treated mouse groups (Figure S10). The ability of HPaCD to decrease PSY levels in the CNS and PNS is likely due to its dual mechanism of action. Beyond the ability to "trap" and neutralize the cytotoxic properties of PSY, HPaCD also promotes PSY clearance by increasing its solubility, resulting in decreased levels where it is most abundant, *i.e.*, CNS and PNS. In fact, while the reductions of PSY levels were noted in CNS and PNS (Figures 5A–5C), concomitant increases of PSY levels in the plasma specimens of HPaCD-treated Twi mice were observed (Figure 5D), indicating PSY clearance from the nervous system. Along these lines, additional experiments demonstrated that HPaCD significantly increases urinary clearance of PSY, as shown in Figure S8. Interestingly, the levels of psychosine in stool specimens from Twi mice, significantly elevated compared with WT age-matched controls, decreased significantly over the treatment period (Figure S8C), supporting the PSY urinary clearance promoted by the HPaCD (Figure S8B).

HPaCD slightly prolonged the Twi lifespan (Figure 6K). Given the short lifespan and severity of the Twi murine KD model, the survival analysis, even though statistically significant (Figure 6K), should be interpreted with caution regarding the therapeutic effect of HPaCD. Nevertheless, because of its dual mechanism of action, HPaCD requires a longer treatment duration, making the early-onset, short-lived Twi mouse an inadequate model for examining the impact of the molecule on survival.[68,69] Consistent with the biochemistry and immunohistochemistry findings, improvements in several neurobehavioral parameters were observed (Figure 6). These phenotypic improvements were corroborated by the ultrastructural axonal morphometric analysis of sciatic nerves of the HPaCD-treated Twi (Figure 7). HPaCD showed to produce significant increases in myelin thickness (Figure 7E), axon diameter (Figure S9A), myelin (Figure 7F), and axon-myelin areas (Figure 7G), axonal and axon-myelin perimeters (Figures S9B and S9C; Table S1). However, no significant differences in axonal density were observed between the HPaCD-treated and vehicle-treated mouse groups (Figure S9D and Table S1). The latter observation is likely related to the significant increases in axonal diameter (Figure S9A) and axonal and axon-myelin areas (Figures 7F and 7G) in the HPaCD-treated mice, not necessarily altering the number of myelinated axons in the nerve fascicle area. The G-ratio is a quantitative measure of relative myelin thickness calculated by the ratio of the inner and outer diameters of the myelin sheath. Abnormalities in myelination can occur in several neurological disorders, including multiple sclerosis, traumatic brain injury, and neurodegenerative diseases.[70,71] As previously reported,[15,60] the G-ratio was statistically increased in the Twi compared to controls (Figure 7H and Table S1). HPaCD promoted significant decreases in the G-ratio of the Twi mice (Figure 7H and Table S1; $p < 0.05$), making this important morphometric parameter not statistically significant differs from WT age-matched controls (Figure 7H and Table S1;$p = 0.316$). The G-ratio increases in the Twi reflects the progressive axonopathy, operating in a "dying-back" pattern, caused by central neuronal dysfunction that occurs concomitantly with the demyelinating process in KD.[72,73]

Regarding safety, the lack of ototoxicity, a complication typically associated with other CDs,[74] can be a potential advantage of HPaCD on clinical grounds. Mice receiving HPaCD at 5,000 mg/kg, the dose tested in the trials, showed no increase in electrophysiological alterations on the acoustic startle response (Figure S7A). In addition, the outer three-cell layer and the inner one-cell layer of hair cells of the cochlear epithelium, as well as the number of support cells in the inner ear, remained intact (Figures S7B and S7C). These findings are consistent with previous studies evaluating HPaCD for potential ototoxicity and studying the mechanism of HPbCD ototoxicity.[74,75] Previously, HPaCD showed no genotoxicity in Ames tests, an *in vivo* mouse bone marrow micronucleus test.[76] No safety concerns were reported in subchronic (13-week) oral toxicity studies in rats and dogs, and embryotoxicity/teratogenicity studies in rats[76] and rabbits.[77] The disposition of this substance was also studied in germ-free and conventional rats.[76]

Beyond the HSCT[12,17] and gene therapy[19,60,78,79] approaches, previous studies have utilized small molecules to target the PSY biosynthetic pathway, potentially serving as therapeutic agents for KD.[7,80] Other small molecules target several inflammatory and promyelinating signaling pathways that contribute to the pathogenesis of KD.[81–86] Similar to the approach reported here, hybrid nanoparticles composed of lecithin/chitosan were shown to prevent the PSY-induced cytotoxicity in cultured human astrocytes *in vitro*[87]. However, no *in vivo* studies using the classical KD models have been reported showing evidence of CNS biodistribution and efficacy.[87]

In sum, this is an innovative therapeutic approach leveraging the properties of HPaCD to molecularly "shield" and neutralize the effects of elevated cytotoxic PSY levels, resulting in improvements in the classical murine KD model (Twi *Galc*$^{twi/twi}$). With a strong safety profile without causing ototoxicity, HPaCD becomes an attractive adjunctive and/or "bridge" therapy in conjunction with the mainstay standard of care (HSCT), and upcoming treatments such as gene therapy. Of utmost importance, several newborn screening programs currently include KD, and an increasing number of individuals with late-onset clinical forms of KD may benefit from early intervention.[88,89] Therefore, the characterization and validation of HPaCD and emerging analogs become highly important adjunctive therapeutic options for improving outcomes in this devastating inborn white matter disorder.

Limitations of the study

The main limitation of the surrogate FITC-αCD molecule is that, despite achieving quantifiable levels in plasma and brain extracts from the murine KD model, the 50 mg/kg dose did not provide sufficient sensitivity to detect FITC-αCD molecules using *in situ* confocal and multiphoton microscopy. Thus, FICT-αCD does not enable the visualization of its brain biodistribution and specific cell penetration. The possibility that the drug adheres to endothelial cells cannot be strictly excluded, although the functional rescue of myelin-forming cells and the reduction of PSY in CNS and PNS suggest valid target engagement. In addition, the heterogeneity in iNSC conversion to Oligos is observed (Figure S4B), which may limit the interpretation of the results. For instance, two mature oligodendrocyte markers, MAG and OSP, showed discrepancies in their expression in cultured iNSC-derived Oligos from a KD patient (Figure S4B). The OSP marker was identified as Claudin-11.[90] Claudins are transmembrane proteins that form tight junctions. OSP/Claudin-11 forms homophilic interactions, establishing tight junctions, which are essential for myelin sheath compaction and stability.[90] Thus, as OSP/Claudin-11 promotes myelin sheath formation, it is expressed later in Oligo maturation, mostly during myelin sheath compaction.[90,91] Since the iNSC-differentiation was not performed in co-culture with neurons or myelination nanofiber matrix, it is conceivable that the high MAG expression in the setting of low OSP expression indicates a particular stage of maturation of iNSC-derived Oligos. Finally, given the short lifespan and severity of the Twi murine KD model, and given the dual mechanism of action of HPaCD, extending treatment duration in this model is not feasible for a thorough examination of the full effects of the proposed molecular therapeutic approach.

RESOURCE AVAILABILITY

Lead contact

All data are available in the main text, figures, tables, or supplemental information. Further inquiries can be directed to the lead contact, Gustavo Maegawa (gm3025@cumc.columbia.edu).

Materials availability

The study did not generate new, or unique reagents.

Data and code availability

- The data reported in this article will be shared by the lead contact upon request.
- No new datasets of a standardized datatype or original codes are reported.
- Any additional information required to reanalyze the data reported in this article is available from the lead contact upon request.

STAR★METHODS

Detailed methods are provided in the online version of this paper and include the following:

- KEY RESOURCES TABLE
- EXPERIMENTAL MODEL AND STUDY PARTICIPANT DETAILS
  - Cell lines
  - Animals
- METHOD DETAILS
  - Cell survival assay
  - Synthesis of FITCαCD
  - Plasma stability and CNS biodistribution of FITC-labeled αCD
  - Animal motor and neurobehavioral tests
  - Automated home cage murine monitoring
  - Rotarod test
  - Open-field evaluations
  - Catwalk
  - Acoustic startle response
  - Survival analysis
  - NMR experiments
  - LC-MS/MS
  - Urinary clearance of PSY
  - Neuropathology specimen preparation and assay allocation
  - Brain sections and immunofluorescence staining
  - Electron microscopy and morphometric analysis
  - TNFα ELISA
- QUANTIFICATION AND STATISTICAL ANALYSIS

ACKNOWLEDGMENTS

We are indebted to Dr. Renu Nandakumar, PhD, Director of the Biomarkers Core Laboratory (BCL) at the Irving Institute for Clinical and Translational Research at Columbia University, who facilitated the availability of instrumentation for implementing and performing the PSY LC-MS/MS assays. We thank Dr. Ernesto Bongarzone and his group at the University of Illinois, Chicago, IL, for sharing the KD Twitcher (*Galc*$^{twi/twi}$) murine line. We also thank Alice Liang, Ph.D., and her team for consultation and timely preparation of the electron microscopy sections and TEM images. We thank Dr. Mu Yang, Ph.D., the Mouse NeuroBehavior Core director at Columbia University, New York, NY, and David Larr, BSc. who assisted in the neurobehavioral evaluations. We are grateful to Mathieu Boudreau and Julien Cohen-Adad, Ph.D., from the NeuroPoly Lab at Polytechnique Montreal, QC, Canada, who provided the training and expertise for the axon and nerve morphometrics analysis using the AxonDeepSeg software. The work was funded by the National Institutes of Health (NIH)/National Institute of Neurological Disorders and Stroke (NINDS), R01NS137638-01 (awarded to GHBM). National Center for Advancing Translational Sciences, National Institutes of Health, through Grant Number UL1TR001873 (Irving Institute for Clinical and Translational Research), Cancer Center Support Grant

NIH/NCI P30CA016087 (partial support for the New York University (NYUHL) Microscopy Lab).

AUTHOR CONTRIBUTIONS

Study design and conceptualization: G.H.B.M. Performed the experiments: E.M.Y.C., J.E., P.Z., S.B., and S.-C.H. Methodology: C.-C.L., E.M.Y.C., G.H.B.M., J.E., M.H.G, S.B., and S.-C.H. Visualization: A.C., C.-C.L., E.K., M.M., G.H.B.M., J.E., M.H.G., and S.-C.H. Data analysis: A.C., C.-C.L., E.K., G.H.B.M., J.E., M.H.G., M.H.M., and S.-C.H. Funding acquisition: G.H.B.M. Project administration: G.H.B.M. Writing – original draft: S.B. and G.H.B.M. Writing – review and editing: C.-C.L., G.H.B.M., M.H.G., and S.B. All authors reviewed the article and approved the submission.

DECLARATION OF INTERESTS

GHBM serves as a consultant for Takeda Pharm., Sanofi, and Chiesi. MHG is a co-founder and member of GelbChem, LLC. The other authors declare no conflicts of interest.

SUPPLEMENTAL INFORMATION

Supplemental information can be found online at https://doi.org/10.1016/j.isci.2026.114808.

Received: August 29, 2025
Revised: November 21, 2025
Accepted: January 20, 2026
Published: January 29, 2026

REFERENCES

1. Igisu, H., and Suzuki, K. (1984). Analysis of galactosylsphingosine (psychosine) in the brain. J. Lipid Res. *25*, 1000–1006.
2. Suzuki, K. (1998). Twenty five years of the "psychosine hypothesis": a personal perspective of its history and present status. Neurochem. Res. *23*, 251–259. https://doi.org/10.1023/a:1022436928925.
3. White, A.B., Galbiati, F., Givogri, M.I., Lopez Rosas, A., Qiu, X., van Breemen, R., and Bongarzone, E.R. (2011). Persistence of psychosine in brain lipid rafts is a limiting factor in the therapeutic recovery of a mouse model for Krabbe disease. J. Neurosci. Res. *89*, 352–364. https://doi.org/10.1002/jnr.22564.
4. Miyatake, T., and Suzuki, K. (1972). Globoid cell leukodystrophy: additional deficiency of psychosine galactosidase. Biochem. Biophys. Res. Commun. *48*, 539–543. https://doi.org/10.1016/0006-291x(72)90381-6.
5. Igisu, H., and Suzuki, K. (1984). Progressive accumulation of toxic metabolite in a genetic leukodystrophy. Science *224*, 753–755. https://doi.org/10.1126/science.6719111.
6. Zaka, M., and Wenger, D.A. (2004). Psychosine-induced apoptosis in a mouse oligodendrocyte progenitor cell line is mediated by caspase activation. Neurosci. Lett. *358*, 205–209. https://doi.org/10.1016/j.neulet.2003.12.126.
7. Li, Y., Xu, Y., Benitez, B.A., Nagree, M.S., Dearborn, J.T., Jiang, X., Guzman, M.A., Woloszynek, J.C., Giaramita, A., Yip, B.K., et al. (2019). Genetic ablation of acid ceramidase in Krabbe disease confirms the psychosine hypothesis and identifies a new therapeutic target. Proc. Natl. Acad. Sci. USA *116*, 20097–20103. https://doi.org/10.1073/pnas.1912108116.
8. Krieg, S.I., Krägeloh-Mann, I., Groeschel, S., Beck-Wödl, S., Husain, R.A., Schöls, L., and Kehrer, C. (2020). Natural history of Krabbe disease - a nationwide study in Germany using clinical and MRI data. Orphanet J. Rare Dis. *15*, 243. https://doi.org/10.1186/s13023-020-01489-3.
9. Pastores, G.M. (2009). Krabbe disease: an overview. Int. J. Clin. Pharmacol. Ther. *47*, S75–S81. https://doi.org/10.5414/cpp47075.
10. Duffner, P.K., Barczykowski, A., Jalal, K., Yan, L., Kay, D.M., and Carter, R.L. (2011). Early infantile Krabbe disease: results of the World-Wide Krabbe Registry. Pediatr. Neurol. *45*, 141–148. https://doi.org/10.1016/j.pediatrneurol.2011.05.007.
11. Duffner, P.K., Barczykowski, A., Kay, D.M., Jalal, K., Yan, L., Abdelhalim, A., Gill, S., Gill, A.L., and Carter, R. (2012). Later onset phenotypes of Krabbe disease: results of the world-wide registry. Pediatr. Neurol. *46*, 298–306. https://doi.org/10.1016/j.pediatrneurol.2012.02.023.
12. Escolar, M.L., Poe, M.D., Provenzale, J.M., Richards, K.C., Allison, J., Wood, S., Wenger, D.A., Pietryga, D., Wall, D., Champagne, M., et al. (2005). Transplantation of umbilical-cord blood in babies with infantile Krabbe's disease. N. Engl. J. Med. *352*, 2069–2081. https://doi.org/10.1056/NEJMoa042604.
13. Page, K.M., Stenger, E.O., Connelly, J.A., Shyr, D., West, T., Wood, S., Case, L., Kester, M., Shim, S., Hammond, L., et al. (2019). Hematopoietic Stem Cell Transplantation to Treat Leukodystrophies: Clinical Practice Guidelines from the Hunter's Hope Leukodystrophy Care Network. Biol. Blood Marrow Transplant. *25*, e363–e374. https://doi.org/10.1016/j.bbmt.2019.09.003.
14. Qin, E.Y., Hawkins-Salsbury, J.A., Jiang, X., Reddy, A.S., Farber, N.B., Ory, D.S., and Sands, M.S. (2012). Bone marrow transplantation increases efficacy of central nervous system-directed enzyme replacement therapy in the murine model of globoid cell leukodystrophy. Mol. Genet. Metab. *107*, 186–196. https://doi.org/10.1016/j.ymgme.2012.05.021.
15. Weinstock, N.I., Shin, D., Dhimal, N., Hong, X., Irons, E.E., Silvestri, N.J., Reed, C.B., Nguyen, D., Sampson, O., Cheng, Y.C., et al. (2020). Macrophages Expressing GALC Improve Peripheral Krabbe Disease by a Mechanism Independent of Cross-Correction. Neuron *107*, 65–81.e9. https://doi.org/10.1016/j.neuron.2020.03.031.
16. Wright, M.D., Poe, M.D., DeRenzo, A., Haldal, S., and Escolar, M.L. (2017). Developmental outcomes of cord blood transplantation for Krabbe disease: A 15-year study. Neurology *89*, 1365–1372. https://doi.org/10.1212/WNL.0000000000004418.
17. Allewelt, H., Taskindoust, M., Troy, J., Page, K., Wood, S., Parikh, S., Prasad, V.K., and Kurtzberg, J. (2018). Long-Term Functional Outcomes after Hematopoietic Stem Cell Transplant for Early Infantile Krabbe Disease. Biol. Blood Marrow Transplant. *24*, 2233–2238. https://doi.org/10.1016/j.bbmt.2018.06.020.
18. Kofler, J., Beltran-Quintero, M.L., Rugari, A., Zuccoli, G., Klotz, S., and Escolar, M.L. (2022). Improved Brain Pathology and Progressive Peripheral Neuropathy in a 15 Year Old Survivor of Infantile Krabbe Disease Treated With Umbilical Cord Transplantation. Front. Mol. Neurosci. *15*, 888231. https://doi.org/10.3389/fnmol.2022.888231.
19. Heller, G., Bradbury, A.M., Sands, M.S., and Bongarzone, E.R. (2023). Preclinical studies in Krabbe disease: A model for the investigation of novel combination therapies for lysosomal storage diseases. Mol. Ther. *31*, 7–23. https://doi.org/10.1016/j.ymthe.2022.09.017.
20. Vecsernyes, M., Fenyvesi, F., Bacskay, I., Deli, M.A., Szente, L., and Fenyvesi, E. (2014). Cyclodextrins, blood-brain barrier, and treatment of neurological diseases. Arch. Med. Res. *45*, 711–729. https://doi.org/10.1016/j.arcmed.2014.11.020.
21. Camargo, F., Erickson, R.P., Garver, W.S., Hossain, G.S., Carbone, P.N., Heidenreich, R.A., and Blanchard, J. (2001). Cyclodextrins in the treatment of a mouse model of Niemann-Pick C disease. Life Sci. *70*, 131–142. https://doi.org/10.1016/s0024-3205(01)01384-4.
22. Ory, D.S., Ottinger, E.A., Farhat, N.Y., King, K.A., Jiang, X., Weissfeld, L., Berry-Kravis, E., Davidson, C.D., Bianconi, S., Keener, L.A., et al. (2017). Intrathecal 2-hydroxypropyl-beta-cyclodextrin decreases neurological disease progression in Niemann-Pick disease, type C1: a non-randomised, open-label, phase 1-2 trial. Lancet *390*, 1758–1768. https://doi.org/10.1016/S0140-6736(17)31465-4.
23. Kunkel, T.J., Townsend, A., Sullivan, K.A., Merlet, J., Schuchman, E.H., Jacobson, D.A., and Lieberman, A.P. (2023). The cholesterol transporter

NPC1 is essential for epigenetic regulation and maturation of oligodendrocyte lineage cells. Nat. Commun. *14*, 3964. https://doi.org/10.1038/s41467-023-39733-6.

24. Ribbens, J.J., Moser, A.B., Hubbard, W.C., Bongarzone, E.R., and Maegawa, G.H.B. (2014). Characterization and application of a disease-cell model for a neurodegenerative lysosomal disease. Mol. Genet. Metab. *111*, 172–183. https://doi.org/10.1016/j.ymgme.2013.09.011.

25. Katabuchi, A.U., Godoy, V., Shil, P., Moser, A., and Maegawa, G.H.B. (2018). Serendipitous effects of beta-cyclodextrin on murine model of Krabbe disease. Mol. Genet. Metab. Rep. *15*, 98–99. https://doi.org/10.1016/j.ymgmr.2018.03.002.

26. Suzuki, K. (2016). My encounters with Krabbe disease: A personal recollection of a 40-Year journey with young colleagues. J. Neurosci. Res. *94*, 965–972. https://doi.org/10.1002/jnr.23735.

27. Banks, W.A., Engelke, K., Hansen, K.M., Bullock, K.M., and Calias, P. (2019). Modest Blood-Brain Barrier Permeability of the Cyclodextrin Kleptose: Modification by Efflux and Luminal Surface Binding. J. Pharmacol. Exp. Ther. *371*, 121–129. https://doi.org/10.1124/jpet.119.260497.

28. Cecchelli, R., Berezowski, V., Lundquist, S., Culot, M., Renftel, M., Dehouck, M.P., and Fenart, L. (2007). Modelling of the blood-brain barrier in drug discovery and development. Nat. Rev. Drug Discov. *6*, 650–661. https://doi.org/10.1038/nrd2368.

29. Cecchelli, R., Dehouck, B., Descamps, L., Fenart, L., Buée-Scherrer, V., V, Duhem, C., Lundquist, S., Rentfel, M., Torpier, G., and Dehouck, M.P. (1999). In vitro model for evaluating drug transport across the blood-brain barrier. Adv. Drug Deliv. Rev. *36*, 165–178. https://doi.org/10.1016/s0169-409x(98)00083-0.

30. Dehouck, M.P., Méresse, S., Delorme, P., Fruchart, J.C., and Cecchelli, R. (1990). An easier, reproducible, and mass-production method to study the blood-brain barrier in vitro. J. Neurochem. *54*, 1798–1801. https://doi.org/10.1111/j.1471-4159.1990.tb01236.x.

31. Monnaert, V., Tilloy, S., Bricout, H., Fenart, L., Cecchelli, R., and Monflier, E. (2004). Behavior of alpha-beta-and gamma-cyclodextrins and their derivatives on an in vitro model of blood-brain barrier. J. Pharmacol. Exp. Ther. *310*, 745–751. https://doi.org/10.1124/jpet.104.067512.

32. Hawkins-Salsbury, J.A., Parameswar, A.R., Jiang, X., Schlesinger, P.H., Bongarzone, E., Ory, D.S., Demchenko, A.V., and Sands, M.S. (2013). Psychosine, the cytotoxic sphingolipid that accumulates in globoid cell leukodystrophy, alters membrane architecture. J. Lipid Res. *54*, 3303–3311. https://doi.org/10.1194/jlr.M039610.

33. Fuchs, T.A., Abed, U., Goosmann, C., Hurwitz, R., Schulze, I., Wahn, V., Weinrauch, Y., Brinkmann, V., and Zychlinsky, A. (2007). Novel cell death program leads to neutrophil extracellular traps. J. Cell Biol. *176*, 231–241. https://doi.org/10.1083/jcb.200606027.

34. Stella, V.J., and He, Q. (2008). Cyclodextrins. Toxicol. Pathol. *36*, 30–42. https://doi.org/10.1177/0192623307310945.

35. Pang, Z.P., Yang, N., Vierbuchen, T., Ostermeier, A., Fuentes, D.R., Yang, T.Q., Citri, A., Sebastiano, V., Marro, S., Südhof, T.C., and Wernig, M. (2011). Induction of human neuronal cells by defined transcription factors. Nature *476*, 220–223. https://doi.org/10.1038/nature10202.

36. Vierbuchen, T., Ostermeier, A., Pang, Z.P., Kokubu, Y., Südhof, T.C., and Wernig, M. (2010). Direct conversion of fibroblasts to functional neurons by defined factors. Nature *463*, 1035–1041. https://doi.org/10.1038/nature08797.

37. Zhu, S., Wang, H., and Ding, S. (2015). Reprogramming fibroblasts toward cardiomyocytes, neural stem cells and hepatocytes by cell activation and signaling-directed lineage conversion. Nat. Protoc. *10*, 959–973. https://doi.org/10.1038/nprot.2015.059.

38. Kano, S., Yuan, M., Cardarelli, R.A., Maegawa, G., Higurashi, N., Gaval-Cruz, M., Wilson, A.M., Tristan, C., Kondo, M.A., Chen, Y., et al. (2015). Clinical utility of neuronal cells directly converted from fibroblasts of patients for neuropsychiatric disorders: studies of lysosomal storage diseases and channelopathy. Curr. Mol. Med. *15*, 138–145. https://doi.org/10.2174/1566524015666150303110300.

39. Liao, H.C., Spacil, Z., Ghomashchi, F., Escolar, M.L., Kurtzberg, J., Orsini, J.J., Turecek, F., Scott, C.R., and Gelb, M.H. (2017). Lymphocyte Galactocerebrosidase Activity by LC-MS/MS for Post-Newborn Screening Evaluation of Krabbe Disease. Clin. Chem. *63*, 1363–1369. https://doi.org/10.1373/clinchem.2016.264952.

40. Douvaras, P., and Fossati, V. (2015). Generation and isolation of oligodendrocyte progenitor cells from human pluripotent stem cells. Nat. Protoc. *10*, 1143–1154. https://doi.org/10.1038/nprot.2015.075.

41. Douvaras, P., Wang, J., Zimmer, M., Hanchuk, S., O'Bara, M.A., Sadiq, S., Sim, F.J., Goldman, J., and Fossati, V. (2014). Efficient generation of myelinating oligodendrocytes from primary progressive multiple sclerosis patients by induced pluripotent stem cells. Stem Cell Rep. *3*, 250–259. https://doi.org/10.1016/j.stemcr.2014.06.012.

42. Wu, D., Chen, Q., Chen, X., Han, F., Chen, Z., and Wang, Y. (2023). The blood-brain barrier: structure, regulation, and drug delivery. Signal Transduct. Target. Ther. *8*, 217. https://doi.org/10.1038/s41392-023-01481-w.

43. Srinivas, N., Maffuid, K., and Kashuba, A.D.M. (2018). Clinical Pharmacokinetics and Pharmacodynamics of Drugs in the Central Nervous System. Clin. Pharmacokinet. *57*, 1059–1074. https://doi.org/10.1007/s40262-018-0632-y.

44. Neumaier, F., Zlatopolskiy, B.D., and Neumaier, B. (2021). Drug Penetration into the Central Nervous System: Pharmacokinetic Concepts and In Vitro Model Systems. Pharmaceutics *13*, 1542. https://doi.org/10.3390/pharmaceutics13101542.

45. Yao, J., Ho, D., Calingasan, N.Y., Pipalia, N.H., Lin, M.T., and Beal, M.F. (2012). Neuroprotection by cyclodextrin in cell and mouse models of Alzheimer disease. J. Exp. Med. *209*, 2501–2513. https://doi.org/10.1084/jem.20121239.

46. Liu, B., Turley, S.D., Burns, D.K., Miller, A.M., Repa, J.J., and Dietschy, J.M. (2009). Reversal of defective lysosomal transport in NPC disease ameliorates liver dysfunction and neurodegeneration in the npc1-/- mouse. Proc. Natl. Acad. Sci. USA *106*, 2377–2382. https://doi.org/10.1073/pnas.0810895106.

47. Davidson, C.D., Ali, N.F., Micsenyi, M.C., Stephney, G., Renault, S., Dobrenis, K., Ory, D.S., Vanier, M.T., and Walkley, S.U. (2009). Chronic cyclodextrin treatment of murine Niemann-Pick C disease ameliorates neuronal cholesterol and glycosphingolipid storage and disease progression. PLoS One *4*, e6951. https://doi.org/10.1371/journal.pone.0006951.

48. Merkus, F.W., Verhoef, J.C., Marttin, E., Romeijn, S.G., van der Kuy, P.H., Hermens, W.A., and Schipper, N.G. (1999). Cyclodextrins in nasal drug delivery. Adv. Drug Deliv. Rev. *36*, 41–57. https://doi.org/10.1016/s0169-409x(98)00054-4.

49. Al Shoyaib, A., Archie, S.R., and Karamyan, V.T. (2019). Intraperitoneal Route of Drug Administration: Should it Be Used in Experimental Animal Studies? Pharm. Res. *37*, 12. https://doi.org/10.1007/s11095-019-2745-x.

50. Montgomery, S.C., and Cox, B.C. (2016). Whole Mount Dissection and Immunofluorescence of the Adult Mouse Cochlea. J. Vis. Exp. *107*, 53561. https://doi.org/10.3791/53561.

51. Davidson, C.D., Fishman, Y.I., Puskás, I., Szemán, J., Sohajda, T., McCauliff, L.A., Sikora, J., Storch, J., Vanier, M.T., Szente, L., et al. (2016). Efficacy and ototoxicity of different cyclodextrins in Niemann-Pick C disease. Ann. Clin. Transl. Neurol. *3*, 366–380. https://doi.org/10.1002/acn3.306.

52. Crumling, M.A., Liu, L., Thomas, P.V., Benson, J., Kanicki, A., Kabara, L., Hälsey, K., Dolan, D., and Duncan, R.K. (2012). Hearing loss and hair cell death in mice given the cholesterol-chelating agent hydroxypropyl-beta-cyclodextrin. PLoS One *7*, e53280. https://doi.org/10.1371/journal.pone.0053280.

53. Cronin, S., Lin, A., Thompson, K., Hoenerhoff, M., and Duncan, R.K. (2015). Hearing Loss and Otopathology Following Systemic and Intracerebroventricular Delivery of 2-Hydroxypropyl-Beta-Cyclodextrin. J. Assoc. Res. Otolaryngol. *16*, 599–611. https://doi.org/10.1007/s10162-015-0528-6.

54. Moore, J.L., Kennedy, J., and Hassan, A.A. (2024). Automated home cage monitoring of an aging colony of mice-Implications for welfare monitoring and experimentation. Front. Neurosci. *18*, 1489308. https://doi.org/10.3389/fnins.2024.1489308.

55. Pernold, K., Iannello, F., Low, B.E., Rigamonti, M., Rosati, G., Scavizzi, F., Wang, J., Raspa, M., Wiles, M.V., and Ulfhake, B. (2019). Towards large scale automated cage monitoring - Diurnal rhythm and impact of interventions on in-cage activity of C57BL/6J mice recorded 24/7 with a non-disrupting capacitive-based technique. PLoS One *14*, e0211063. https://doi.org/10.1371/journal.pone.0211063.

56. Barmann, J., Walter, H.L., Pikhovych, A., Endepols, H., Fink, G.R., Rueger, M.A., and Schroeter, M. (2021). An analysis of the CatWalk XT and a composite score to assess neurofunctional deficits after photothrombosis in mice. Neurosci. Lett. *751*, 135811. https://doi.org/10.1016/j.neulet.2021.135811.

57. Zheng, G., Zhang, H., Tail, M., Wang, H., Walter, J., Skutella, T., Unterberg, A., Zweckberger, K., and Younsi, A. (2023). Assessment of hindlimb motor recovery after severe thoracic spinal cord injury in rats: classification of CatWalk XT(R) gait analysis parameters. Neural Regen. Res. *18*, 1084–1089. https://doi.org/10.4103/1673-5374.355763.

58. Zaimi, A., Wabartha, M., Herman, V., Antonsanti, P.L., Perone, C.S., and Cohen-Adad, J. (2018). AxonDeepSeg: automatic axon and myelin segmentation from microscopy data using convolutional neural networks. Sci. Rep. *8*, 3816. https://doi.org/10.1038/s41598-018-22181-4.

59. Cappello, V., Marchetti, L., Parlanti, P., Landi, S., Tonazzini, I., Cecchini, M., Piazza, V., and Gemmi, M. (2016). Ultrastructural Characterization of the Lower Motor System in a Mouse Model of Krabbe Disease. Sci. Rep. *6*, 1. https://doi.org/10.1038/s41598-016-0001-8.

60. Marshall, M.S., Issa, Y., Jakubauskas, B., Stoskute, M., Elackattu, V., Marshall, J.N., Bogue, W., Nguyen, D., Hauck, Z., Rue, E., et al. (2018). Long-Term Improvement of Neurological Signs and Metabolic Dysfunction in a Mouse Model of Krabbe's Disease after Global Gene Therapy. Mol. Ther. *26*, 874–889. https://doi.org/10.1016/j.ymthe.2018.01.009.

61. Coletti, H.Y., Aldenhoven, M., Yelin, K., Poe, M.D., Kurtzberg, J., and Escolar, M.L. (2015). Long-term functional outcomes of children with hurler syndrome treated with unrelated umbilical cord blood transplantation. JIMD Rep. *20*, 77–86. https://doi.org/10.1007/8904_2014_395.

62. Kwon, J.M., Matern, D., Kurtzberg, J., Wrabetz, L., Gelb, M.H., Wenger, D.A., Ficicioglu, C., Waldman, A.T., Burton, B.K., Hopkins, P.V., and Orsini, J.J. (2018). Consensus guidelines for newborn screening, diagnosis and treatment of infantile Krabbe disease. Orphanet J. Rare Dis. *13*, 30. https://doi.org/10.1186/s13023-018-0766-x.

63. Li, Y., Miller, C.A., Shea, L.K., Jiang, X., Guzman, M.A., Chandler, R.J., Ramakrishnan, S.M., Smith, S.N., Venditti, C.P., Vogler, C.A., et al. (2021). Enhanced Efficacy and Increased Long-Term Toxicity of CNS-Directed, AAV-Based Combination Therapy for Krabbe Disease. Mol. Ther. *29*, 691–701. https://doi.org/10.1016/j.ymthe.2020.12.031.

64. Hennrich, N., and Cramer, F. (1965). Inclusion Compounds. 18. The Catalysis of the Fission of Pyrophosphates by Cyclodextrin. A Model Reaction for the Mechanism of Enzymes. J. Am. Chem. Soc. *87*, 1121–1126. https://doi.org/10.1021/ja01083a032.

65. Kiss, T., Fenyvesi, F., Bácskay, I., Váradi, J., Fenyvesi, E., Iványi, R., Szente, L., Tósaki, A., and Vecsernyés, M. (2010). Evaluation of the cytotoxicity of beta-cyclodextrin derivatives: evidence for the role of cholesterol extraction. Eur. J. Pharm. Sci. *40*, 376–380. https://doi.org/10.1016/j.ejps.2010.04.014.

66. Zavitsas, A.A. (2009). The Relation between Bond Lengths and Dissociation Energies of Carbon-Carbon Bonds (vol 107, pg 898, 2003). J. Phys. Chem. A *113*, 1403. https://doi.org/10.1021/jp900553q.

67. Varadi, J., Hermenean, A., Gesztelyi, R., Jeney, V., Balogh, E., Majoros, L., Malanga, M., Fenyvesi, E., Szente, L., Bacskay, I., et al. (2019). Pharmacokinetic Properties of Fluorescently Labelled Hydroxypropyl-Beta-Cyclodextrin. Biomolecules *9*, 509. https://doi.org/10.3390/biom9100509.

68. Duchen, L.W., Eicher, E.M., Jacobs, J.M., Scaravilli, F., and Teixeira, F. (1980). Hereditary leucodystrophy in the mouse: the new mutant twitcher. Brain *103*, 695–710. https://doi.org/10.1093/brain/103.3.695.

69. Kobayashi, T., Yamanaka, T., Jacobs, J.M., Teixeira, F., and Suzuki, K. (1980). The Twitcher mouse: an enzymatically authentic model of human globoid cell leukodystrophy (Krabbe disease). Brain Res. *202*, 479–483. https://doi.org/10.1016/0006-8993(80)90159-6.

70. Chomiak, T., and Hu, B. (2009). What is the optimal value of the g-ratio for myelinated fibers in the rat CNS? A theoretical approach. PLoS One *4*, e7754. https://doi.org/10.1371/journal.pone.0007754.

71. Fields, R.D. (2008). White matter in learning, cognition and psychiatric disorders. Trends Neurosci. *31*, 361–370. https://doi.org/10.1016/j.tins.2008.04.001.

72. Castelvetri, L.C., Givogri, M.I., Zhu, H., Smith, B., Lopez-Rosas, A., Qiu, X., van Breemen, R., and Bongarzone, E.R. (2011). Axonopathy is a compounding factor in the pathogenesis of Krabbe disease. Acta Neuropathol. *122*, 35–48. https://doi.org/10.1007/s00401-011-0814-2.

73. Teixeira, C.A., Miranda, C.O., Sousa, V.F., Santos, T.E., Malheiro, A.R., Solomon, M., Maegawa, G.H., Brites, P., and Sousa, M.M. (2014). Early axonal loss accompanied by impaired endocytosis, abnormal axonal transport, and decreased microtubule stability occur in the model of Krabbe's disease. Neurobiol. Dis. *66*, 92–103. https://doi.org/10.1016/j.nbd.2014.02.012.

74. Bar, A., Krul, C.A., Jonker, D., and de Vogel, N. (2004). Safety evaluation of an alpha-cyclodextrin glycosyltranferase preparation. Regul. Toxicol. Pharmacol. *39*, S47–S56. https://doi.org/10.1016/j.yrtph.2004.05.009.

75. Yamada, Y., Tanaka, M., Ikeda, Y., Kondo, Y., Takeo, T., Nakagata, N., Miwa, T., Takeda, H., Orita, Y., Motoyama, K., et al. (2025). Inability of alpha-cyclodextrins to accommodate cholesterol potentially underlies their lack of efficacy and ototoxicity in Niemann-Pick disease type C treatment. Sci. Rep. *15*, 30857. https://doi.org/10.1038/s41598-025-15599-0.

76. Waalkens-Berendsen, D.H., and Bär, A. (2004). Embryotoxicity and teratogenicity study with alpha-cyclodextrin in rats. Regul. Toxicol. Pharmacol. *39*, S34–S39. https://doi.org/10.1016/j.yrtph.2004.05.004.

77. Waalkens-Berendsen, D.H., Smits-Van Prooije, A.E., and Bär, A. (2004). Embryotoxicity and teratogenicity study with alpha-cyclodextrin in rabbits. Regul. Toxicol. Pharmacol. *39*, S40–S46. https://doi.org/10.1016/j.yrtph.2004.05.003.

78. Bradbury, A.M., Bagel, J.H., Nguyen, D., Lykken, E.A., Pesayco Salvador, J., Jiang, X., Swain, G.P., Assenmacher, C.A., Hendricks, I.J., Miyadera, K., et al. (2020). Krabbe disease successfully treated via monotherapy of intrathecal gene therapy. J. Clin. Investig. *130*, 4906–4920. https://doi.org/10.1172/JCI133953.

79. Hawkins-Salsbury, J.A., Shea, L., Jiang, X., Hunter, D.A., Guzman, A.M., Reddy, A.S., Qin, E.Y., Li, Y., Gray, S.J., Ory, D.S., and Sands, M.S. (2015). Mechanism-based combination treatment dramatically increases therapeutic efficacy in murine globoid cell leukodystrophy. J. Neurosci. *35*, 6495–6505. https://doi.org/10.1523/JNEUROSCI.4199-14.2015.

80. LeVine, S.M., Pedchenko, T.V., Bronshteyn, I.G., and Pinson, D.M. (2000). L-cycloserine slows the clinical and pathological course in mice with globoid cell leukodystrophy (twitcher mice). J. Neurosci. Res. *60*, 231–236. https://doi.org/10.1002/(SICI)1097-4547(20000415)60:2<231::AID-JNR12>3.0.CO;2-E.

81. Potter, G.B., and Petryniak, M.A. (2016). Neuroimmune mechanisms in Krabbe's disease. J. Neurosci. Res. *94*, 1341–1348. https://doi.org/10.1002/jnr.23804.

82. Inamura, N., Kawai, T., Watanabe, T., Aoki, H., Aoyama, M., Nakayama, A., Matsuda, J., and Enokido, Y. (2024). Promyelinating drugs ameliorate

oligodendrocyte pathologies in a mouse model of Krabbe disease. Mol. Genet. Metab. *142*, 108497. https://doi.org/10.1016/j.ymgme.2024.108497.

83. Bechet, S., O'Sullivan, S.A., Yssel, J., Fagan, S.G., and Dev, K.K. (2020). Fingolimod Rescues Demyelination in a Mouse Model of Krabbe's Disease. J. Neurosci. *40*, 3104–3118. https://doi.org/10.1523/JNEUROSCI.2346-19.2020.
84. Papakyriakopoulou, P., Balafas, E., Kostomitsopoulos, N., Rekkas, D.M., Dev, K.K., and Valsami, G. (2024). Pharmacokinetic Study of Fingolimod Nasal Films Administered via Nose-to-Brain Route in C57BL/6 J Mice as Potential Treatment for Multiple Sclerosis. Pharm. Res. *41*, 1951–1963. https://doi.org/10.1007/s11095-024-03745-8.
85. Papakyriakopoulou, P., Valsami, G., and Dev, K.K. (2024). The Effect of Donepezil Hydrochloride in the Twitcher Mouse Model of Krabbe Disease. Mol. Neurobiol. *61*, 8688–8701. https://doi.org/10.1007/s12035-024-04137-0.
86. Braz, S.O., Morgado, M.M., Pereira, M.I., Monteiro, A.C., Golonzhka, O., Jarpe, M., Brites, P., Sousa, M.M., and Nogueira-Rodrigues, J. (2023). HDAC-6 inhibition ameliorates the early neuropathology in a mouse model of Krabbe disease. Front. Mol. Neurosci. *16*, 1231659. https://doi.org/10.3389/fnmol.2023.1231659.
87. Clementino, A., Velasco-Estevez, M., Buttini, F., Sonvico, F., and Dev, K.K. (2021). Hybrid Nanoparticles as a Novel Tool for Regulating Psychosine-Induced Neuroinflammation and Demyelination In Vitro and Ex vivo. Neurotherapeutics *18*, 2608–2622. https://doi.org/10.1007/s13311-021-01109-3.
88. Ream, M.A., Lam, W.K.K., Grosse, S.D., Ojodu, J., Jones, E., Prosser, L.A., Rose, A.M., Marie Comeau, A., Tanksley, S., DiCostanzo, K.P., and Kemper, A.R. (2025). Evidence and Recommendation for Infantile Krabbe Disease Newborn Screening. Pediatrics *155*, e2024069152. https://doi.org/10.1542/peds.2024-069152.
89. Matern, D., Basheeruddin, K., Klug, T.L., McKee, G., Edge, P.U., Hall, P.L., Kurtzberg, J., and Orsini, J.J. (2024). Newborn Screening for Krabbe Disease: Status Quo and Recommendations for Improvements. Int. J. Neonatal Screen. *10*, 10. https://doi.org/10.3390/ijns10010010.
90. Bronstein, J.M., Chen, K., Tiwari-Woodruff, S., and Kornblum, H.I. (2000). Developmental expression of OSP/claudin-11. J. Neurosci. Res. *60*, 284–290. https://doi.org/10.1002/(SICI)1097-4547(20000501)60:3<284::AID-JNR2>3.0.CO;2-T.
91. Gjervan, S.C., Ozgoren, O.K., Gow, A., Stockler-Ipsiroglu, S., and Pouladi, M.A. (2023). Claudin-11 in health and disease: implications for myelin disorders, hearing, and fertility. Front. Cell. Neurosci. *17*, 1344090. https://doi.org/10.3389/fncel.2023.1344090.
92. Sakai, N., Inui, K., Tatsumi, N., Fukushima, H., Nishigaki, T., Taniike, M., Nishimoto, J., Tsukamoto, H., Yanagihara, I., Ozono, K., and Okada, S. (1996). Molecular cloning and expression of cDNA for murine galactocerebrosidase and mutation analysis of the twitcher mouse, a model of Krabbe's disease. J. Neurochem. *66*, 1118–1124.
93. Melton, L.D., and Slessor, K.N. (1971). Synthesis of Monosubstituted Cyclohexaamyloses. Carbohydr. Res. *18*, 29–37. https://doi.org/10.1016/S0008-6215(00)80256-6.
94. Leblanc, A.F., Huang, K.M., Uddin, M.E., Anderson, J.T., Chen, M., and Hu, S. (2018). Murine Pharmacokinetic Studies. Bio. Protoc. *8*, e3056. https://doi.org/10.21769/BioProtoc.3056.
95. Colombo, S., Reddy, H.P., Petri, S., Williams, D.J., Shalomov, B., Dhindsa, R.S., Gelfman, S., Krizay, D., Bera, A.K., Yang, M., et al. (2023). Epilepsy in a mouse model of GNB1 encephalopathy arises from altered potassium (GIRK) channel signaling and is alleviated by a GIRK inhibitor. Front. Cell. Neurosci. *17*, 1175895. https://doi.org/10.3389/fncel.2023.1175895.
96. Kraeuter, A.K., Guest, P.C., and Sarnyai, Z. (2019). The Open Field Test for Measuring Locomotor Activity and Anxiety-Like Behavior. Methods Mol. Biol. *1916*, 99–103. https://doi.org/10.1007/978-1-4939-8994-2_9.
97. Cho, J.D., Kim, Y.A., Rafikian, E.E., Yang, M., and Santa-Maria, I. (2021). Marked Mild Cognitive Deficits in Humanized Mouse Model of Alzheimer's-Type Tau Pathology. Front. Behav. Neurosci. *15*, 634157. https://doi.org/10.3389/fnbeh.2021.634157.
98. Ressler, A.K., Sampaio, G.L.A., Dugger, S.A., Sapir, T., Krizay, D., Boland, M.J., Reiner, O., and Goldstein, D.B. (2023). Evidence of shared transcriptomic dysregulation of HNRNPU-related disorder between human organoids and embryonic mice. iScience *26*, 105797. https://doi.org/10.1016/j.isci.2022.105797.
99. Dugger, S.A., Dhindsa, R.S., Sampaio, G.D.A., Ressler, A.K., Rafikian, E.E., Petri, S., Letts, V.A., Teoh, J., Ye, J., Colombo, S., et al. (2023). Neurodevelopmental deficits and cell-type-specific transcriptomic perturbations in a mouse model of HNRNPU haploinsufficiency. PLoS Genet. *19*, e1010952. https://doi.org/10.1371/journal.pgen.1010952.
100. Hwang, T.L., and Shaka, A.J. (1995). Water Suppression That Works. Excitation Sculpting Using Arbitrary Wave-Forms and Pulsed-Field Gradients. J. Magn. Reson., Ser. A *112*, 275–279.
101. Stechman, M.J., Ahmad, B.N., Loh, N.Y., Reed, A.A.C., Stewart, M., Wells, S., Hough, T., Bentley, L., Cox, R.D., Brown, S.D.M., and Thakker, R.V. (2010). Establishing normal plasma and 24-hour urinary biochemistry ranges in C3H, BALB/c and C57BL/6J mice following acclimatization in metabolic cages. Lab. Anim. *44*, 218–225. https://doi.org/10.1258/la.2010.009128.
102. Kim, A.K., and Hill, W.G. (2017). Effect of filling rate on cystometric parameters in young and middle aged mice. Bladder (San Franc) *4*, e28. https://doi.org/10.14440/bladder.2017.88.
103. de Vito, G., Cappello, V., Tonazzini, I., Cecchini, M., and Piazza, V. (2017). RP-CARS reveals molecular spatial order anomalies in myelin of an animal model of Krabbe disease. J. Biophotonics *10*, 385–393. https://doi.org/10.1002/jbio.201500305.

STAR★METHODS

KEY RESOURCES TABLE

REAGENT or RESOURCE	SOURCE	IDENTIFIER
Antibodies		
Rabbit anti-glial fibrillary acidic protein (GFAP)	Encor Biotechnology Inc.	catalog#RPCA-GFAP
Goat anti-myelin basic protein (MBP)	Encor Biotechnology Inc.	catalog# GPCA-MBP
Mouse monoclonal anti-myelin basic protein (MBP), aa 82–87	EMD Millipore-Sigma	catalog# MAB386
Rabbit Polyclonal anti-Myosin-7A antibody	Proteintech	catalog#20720-1-AP
Goat Polyclonal anti-Sox2 antibody	Santa Cruz Biotech.	catalog#sc-17320
Chemicals, peptides, and recombinant proteins		
Galactosyl(ß) Sphingosine (d18:1)	AvantiResearch	Catalog#860537; CAS#2238-90-6; MW 461.63
Galactosyl(β) Sphingosine-d5	AvantiResearch	Cat# 330714; MW 466.663
2-Hydroxypropyl-α-cyclodextrin (HPaCD)	Millipore-Sigma	CAS#128446-33-3; Cat#390690; MW ∼1,380
2-Hydroxypropyl-β-cyclodextrin (HPbCD)	Millipore-Sigma	CAS#128446-35-5; Cat# 332593; MW ∼1,460
2-Hydroxypropyl-γ-cyclodextrin (HPgCD)	Millipore-Sigma	CAS#128446-34-4; Cat# 779229; MW ∼1,580
heptakis(2,6-di-*O*-methyl)-βCD (DM-b-CD)	Millipore-Sigma	CAS#128446-34-4; Cat# 51166-71-3; MW ∼1,580
FITC-αCD conjugate 6 (PZ11080)	This paper	N/A
heptakis(2,6-di-*O*-methyl)-βCD (DM-b-CD) -	Millipore-Sigma	CAS#128446-34-4; Cat# 51166-71-3; MW ∼1,580
FITC-αCD conjugate 6 (PZ11080)	This paper	N/A
Human dermal fibroblast Nucleofector kit	Lonza	Cat#VAPD-1001
Advanced DMEM/F-12	Life Technologies	Cat#12634-028
Neurobasal medium	Life Technologies	Cat#21103-049
Lysophosphatidic acid	Santa Cruz Biotech; Zhu et al., 2015[36]	Cat#sc-201053
Rolipram	Tocris; Zhu et al., 2015[36]	Cat#0905
SP600125	Tocris; Zhu et al., 2015[36]	Cat#1496
Matrigel	BD Biosciences	Cat# 354230
N-2 supplement (N2), 100×	Life Technologies	Cat#17502-048
B-27 serum-free supplement, (50×)	Life Technologies	Cat#17504-044
B27 Supplement without VitA (50 x)	Life Technologies	Cat#12587-010
A83-01	Stemgent; Zhu et al., 2015[36]	Cat#04-0005
CHIR99021	Tocris; Zhu et al., 2015[36]	Cat#4423
Thiazovivin	Stemgent; Zhu et al., 2015[36]	Cat#04-0017
β-Mercaptoethanol, (55mM; 1,000×)	Life Technologies; Zhu et al., 2015[36]	Cat#21985-023
All-trans retinoic acid (RA)	Millipore-Sigma; Method described in Douvratas et al., 2015[36]	Cat# R2625
SB431542	Stemgent; Method described in Douvratas et al., 2015[36]	Cat# 04-0010
LDN-193189	Stemgent; Method described in Douvratas et al., 2015[36]	Cat#04-0074
Smoothened agonist (SAG)	Millipore-Sigma; Method described in Douvratas et al., 2015[36]	Cat#566660
Recombinant human PDGF-AA, CF	R&D Systems; Method described in Douvratas et al., 2015[36]	Cat#221-AA-050
Recombinant human IGF-I, CF	R&D Systems; Method described in Douvratas et al., 2015[36]	Cat# 291-G1-200
Recombinant human HGF	R&D Systems; Method described in Douvratas et al., 2015[36]	Cat# 294-HG-025

(*Continued on next page*)

Continued

REAGENT or RESOURCE	SOURCE	IDENTIFIER
Neurotrophin 3 (NT3)	EMD Millipore; Method described in Douvratas et al., 2015[36]	Cat# GF031
Insulin solution, human	Millipore-Sigma; Method described in Douvratas et al., 2015[36]	Cat# 19278
Biotin	Millipore-Sigma; Method described in Douvratas et al., 2015[36]	Cat# 4639
*N*6,2′-O-Dibutyryladenosine 3′,5′-cyclic monophosphate sodium salt (cAMP analog)	Millipore-Sigma; Method described in Douvratas et al., 2015[36]	Cat# D0260
3,3,5-Triiodo-l-thyronine (T3)	Millipore-Sigma; Method described in Douvratas et al., 2015[36]	Cat# T2877
All-trans retinoic acid (RA)	Millipore-Sigma; Method described in Douvratas et al., 2015[36]	Cat# R2625
L-Ascorbic acid (AA)	Millipore-Sigma; Method described in Douvratas et al., 2015[36]	Cat# A4403
Poly-l-ornithine hydrobromide	Millipore-Sigma	Cat# 3655
Critical commercial assays		
Calcein Blue, AM – live cell assay	Invitrogen – Psychosine Cytotoxicity Assay (this paper)	Cat#C1429
Ethidium Homodimer III (EthD-III) – dead cell assay	Biotium™– Psychosine Cytotoxicity Assay (this paper)	Cat#40050
2′-(4-Ethoxyphenyl)-5-(4-methyl-1-piperazinyl)-2,5′-bi-1H-benzimidazole trihydrochloride	Millipore-Sigma	Cat#14533
Deposited data		
Raw data shown in figures and supplemental materials	This paper; Mendeley Data	https://data.mendeley.com/preview/z43j2xrhy3?a=bf4f26b8-bd0c-4bcf-99e5-0ea7ec968b5c
Experimental models: Cell lines		
Murine: neuroglial cell line	This group. Described in Ribbens JJ et al. 2014	145M-Twi
Murine: neuroglial cell line	This group. Described in Ribbens JJ et al. 2014[24]	145C-WT
Human-induced stem cells (hiNSC)	This paper. Method described in Zhu et al., 2015[36]	hiNSC-LOKD hiNSC-EOKD hiNSC-CTRL
hiNSC-derived oligodendrocytes	This paper. Method described in Douvratas et al., 2015[36]	hiNSC-Oligo-LOKD hiNSC-Oligo-EOKD hiNSC-Oligo-CTRL
Human: Primary fibroblasts Krabbe disease patient	This paper.	h-LOKD h-EOKD h-CTRL
Experimental models: Organisms/strains		
Mouse: B6.CE-Galctwi/J (Twitcher)	The Jackson Laboratory	Strain #:000845 RRID:IMSR_JAX:000845
Mouse: C57BL/6J (Wild type)	The Jackson Laboratory	Strain #:000664 RRID:IMSR_JAX:000664
Oligonucleotides		
qPCR Oligos: Myelin-Associated Glycoprotein (MAG) (MAG Fwd.: TCTGGATTATGATTTCAGCC; MAG Rev: GTAGAAACGGTTTTCACCAA)	This paper	N/A

(*Continued on next page*)

Continued

REAGENT or RESOURCE	SOURCE	IDENTIFIER
qPCR Oligos: Oligodendrocyte-Specific Protein (OSP) (OSP Fwd.: ACTGCT GCTGACTGTTCTTC; OSP Rev.: GTAGAAACGGTTTTCACCAA)	This paper	N/A
qPCR Oligos: Oligodencrocyte-2 (Oligo2) Fwd.: GCAGAGCACTGC ACTTGACTTCTT; Oligo2 Rev.: CTTCTGCAGTGCGGTT CCTG)	This paper	N/A
Recombinant DNA		
Episomal Plasmids: pCXLE-hOCT3/4-shp53 for primary conversion to iNSC	Addgene; Described in Zhu et al. 2015[36]	cat# 27077
Episomal Plasmids: pCXLE-hSK for primary conversion to iNSC	Addgene; Described in Zhu et al. 2015[36]	cat# 27078
Episomal Plasmids: pCXLE-EGFP for primary conversion to iNSC	Addgene; Described in Zhu et al. 2015[36]	cat# 27078
Software and algorithms		
AxonDeep Seg - v5.1.1 (2025-07-02) AxonDeepSeg is an open-source software using deep learning and aiming at automatically segmenting axons and myelin sheaths from microscopy images. It performs multi-class semantic segmentation using a convolutional neural network.	Zaimi A et al.[55] To reach lead contact for raw files on the images of morphometric analysis.	https://axondeepseg.readthedocs.io/en/latest/documentation.html

EXPERIMENTAL MODEL AND STUDY PARTICIPANT DETAILS

Cell lines

Primary fibroblasts were established from skin biopsies of individuals with or without a diagnosis of KD and healthy controls, under a local IRB-approved protocol at Columbia University Irving Medical Center in New York, NY (IRB#AAAU-0109). Cell lines were previously authenticated by morphological and classical markers. Cells were cultured in T75 cm^2 flasks, subsequently trypsinized, and re-seeded into 96-well tissue culture plates for further experiments. The cells were cultured in DMEM (Sigma-Aldrich, D6546), high glucose supplemented by 10% fetal bovine serum (FBS) and 1% penicillin/streptomycin (P/S; 100 μg/mL). For the experiments, lower passage numbers were used (< 6 passages).

The neuroglial 145M-Twi and 145C-WT obtained from neonatal cortices from Twi *Galc*$^{twi/twi}$ and wild-type C57BL6 *Galc*$^{wt/wt}$ mice, respectively, were cultured in DMEM/F12 with 10%FBS and 1% PS, as previously authenticated, and described by our group.[24] The human-induced stem cells (hiNSC) were established from KD patient-derived primary fibroblasts, as previously described by Zhu and Ding, 2015.[37] The hiNSCs were then used to differentiate into cultured oligodendrocyte-progenitor cells (OPCs), as described in Douvratas et al. 2015.[40] These iNSC KD Oligodendrocytes were isolated by centrifuging the cell suspension into a 15% bovine serum albumin (BSA; Sigma-Aldrich, A3294) cushion for 10 minutes at 1000 rpm. Cells were then resuspended in DMEM: F12 supplemented with 1% P/S, 2× B27 (Invitrogen, 0080085SA), 2 mM L-glutamine (L-Glu; Invitrogen, 25030024), and 50 ng/mL nerve growth factor (NGF; Merck Millipore, 01-125).

All cell lines were tested routinely for mycoplasma contamination.

Animals

Wild type (WT, *Galc*$^{wt/wt}$) and Twitcher (Twi, *Galc*^{twitwi}) mice were identified via PCR, as previously described,[92] and all were maintained on a C57BL/6J background. Males and females were used in the described experiments and randomly assigned to different treatment groups. Neonatal Twi mice (postnatal day, PND, 2-3) were treated with 2-hydroxypropyl-α-CD (HPaCD), which was prepared in PBS at a final concentration of 300 mg/mL. Starting at postnatal day (PND) 2-3, Twi mice were injected intraperitoneally (i.p.) every day (5000 mg/kg) with either HPaCD or vehicle (PBS) and euthanized at PND 36-38 (n=12 for each condition). The intraperitoneal (i.p.) injections were delivered using a 28G insulin syringe. After treatments, the mice were returned to their home cage with their mother. Any treated mice that died within 2 days of the injections were excluded from this study. Animals were monitored twice weekly until PND 36-38, and health condition parameters were scored, including weight loss, natural/provoked behavior, and activity level. Natural behavior was assessed by observing the animal in its home cage, where it exhibited normal mobility. Animal

work in this study was performed following approved protocols and ethical guidelines from the Institutional Animal Care and Use Committee at the Columbia University Irving Medical Center in New York, NY (Protocol#AC-AABP7562). The experimental procedures were conducted in accordance with the ARRIVE guidelines.

METHOD DETAILS

Cell survival assay

PSY used for cytotoxicity experiments was purchased from AvantiResearch (Galactosyl(ß) Sphingosine (d18:1); $C_{24}H_{47}NO_7$; MW 461.63). To confirm the cytoprotection effects of HPaCD, the calcein AM Blue (blue live-cell stain)/ethidium homodimer III (EthD-III; red dead-cell stain) cell survival assay was used to precisely ascertain the number of live and dead cultured fibroblasts pre-treated with HPaCD, followed by PSY challenge (Figure 2A). The non-fluorescent calcein AM permeates the intact fibroblast membrane and is converted into the fluorescent calcein by intracellular esterases.[33] Thus, live primary cultured fibroblasts are indicated by the intensity of blue fluorescence in the cytosol (ex360 nm/em 445 nm). EthD-III is virtually nonfluorescent and impermeant to an intact fibroblast plasma membrane. In the event of compromised cell membrane integrity associated with cell death, EthD-III enters cells, and binds to nucleic acids, resulting in red fluorescence in dead cells (ex 530 nm/em 645 nm).

Synthesis of FITCαCD

The fluorescent FITC-αCD conjugate 6 (PZ11081) was synthesized according to the scheme in Figure S3, using commercially available α-CD (**1**) as the starting material. By following previously described procedures,[93] αCD (**1**) was first monotosylated at one of the 6-positions, to afford the desired 6-monotosylate intermediate **2.** Then the 6-tosyl leaving group was displaced with sodium azide in *N*,*N*-dimethylformamide at 80°C to obtain the corresponding mono-6-azido-6-deoxy-αCD (**3**), which was reduced by a catalytic hydrogenolysis using 5% Pd/C as a catalyst to obtain the desired mono-6-amino-6-deoxy-α-CD (**4**). With the key compound **4** in hand, we carried out a final conjugation with the commercially available fluorescein-isothiocyanate isomer I (**5**, 2.0 equiv. per amine) in *N*,*N*-dimethylformamide in the presence of sodium bicarbonate as a base. After stirring overnight, the desired FITC-αCD conjugate **6** (PZ11080) was isolated by reverse-phase column chromatography on C18 in 54% yield.

Regarding the experimental steps numbered and depicted in Figure S3, to A solution of mono-6-amino-6-deoxy-αCD (**4**, 50 mg, 0.051 mmol)[93] in *N*,*N*-dimethylformamide (1.0 mL), was added $NaHCO_3$ (22 mg, 0.26 mmol) followed by fluorescein isothiocyanate isomer I (40 mg, 0.103 mmol). The reaction was stirred at room temperature overnight and then concentrated in a *vacuum*. The crude residue was purified by reverse-phase chromatography on C18 using a gradient of H_2O - MeOH (0% →50%, v/v) as the eluent to yield the fluorescent FITC-αCD **6** (38 mg, 54%). ^{1}H-NMR (400 MHz, D_2O) δ 7.64 – 7.51 (m, 2H, Ar), 7.28 (d, J = 8.2 Hz, 1H, Ar), 7.16 (dd, J = 9.8, 7.0 Hz, 2H, Ar), 6.55 (m, 4H, Ar), 5.04 (d, J = 3.6 Hz, 1H, H-1), 5.01 – 4.88 (m, 4H, 4 × H-1), ~4.73 (overlapped with HDO, 1H, H-1) 4.38 – 3.20 (m, 36H, 6 × H-2, 6 × H-3, 6 × H-4, 6 × H-5, 6 × H-6a, 6 × H-6b). HRMS (ESI-QTOF) calc'd *m/z* for $C_{57}H_{73}N_2O_{34}S$ $(M+H]^+$: 1361.3765; found: 1361.3706. Calc'd *m/z* for $C_{57}H_{72}N_2O_{34}SNa$ $(M+Na]^+$: 1383.3585; found: 1383.3544.

Plasma stability and CNS biodistribution of FITC-labeled αCD

In vivo stability and CNS biodistribution of the FITC-labeled αCD were conducted in the Twi *Galc*$^{twi/twi}$ mouse line. Six mice (3 males and 3 females) at 30 postnatal days (PND) were used for the experiment. A 50 mg/kg dose of the FITC-labeled αCD was administered intravenously (IV) to the six mice. For the PK sampling, blood samples were collected at times 0, 1, 2, 4.5, and 24 hrs post-single dose administration. As previously described, the blood samples were collected by retro-orbital punctures and the final (post-24 h) through intracardiac puncture.[94] A 500-800 mL volume of blood/mouse was collected in a sodium heparin tube. The mice were euthanized, and their whole bodies were perfused with heparinized saline (0.9% NaCl with 10,000 IU/L of heparin). The brains were homogenized by adding 750 mL PBS solution, and the homogenates were centrifuged at 10,000 rpm for 20 min at 4°C. Plasma samples were diluted 1:5 in PBS. From each sample, 100 mL per well of brain supernatants and 100 mL of diluted plasma were placed into black solid-bottom 96-well plates, and the fluorescence intensities (ex 488/em 530) were measured by Cytation5 (multifunctional plate reader as described above. The protein content of the brain homogenates and 1:5 diluted plasma samples was determined by BCA protein assay (Thermo Scientific, Rockford, IL, USA). The FITC-labeled αCD content of the samples was normalized to the tissue protein content.

Animal motor and neurobehavioral tests

For the neurobehavioral assessments, mice were divided into three groups: HPaCD-treated (n=12; 6 males, 6 females), vehicle-treated (n=12; 6 males, 6 females), and wild-type (n=4). Figure 7A depicts the sketch of the study plan.

Automated home cage murine monitoring

The Digital Ventilated Cage (DVC) system (Tecniplast SpA, Italy) allows for continuous recording of home cage locomotor activity.[54] The study used black Individually Ventilated Cages (IVCs) equipped with individual cool white LED system known as Leddy. As per DVC protocol guidelines, a set of 2 cages, each housing two animals from the same cohort – either HPaCD-treated, vehicle-treated, or WT - were housed in each IVC for 7 days from PND 23 to 29. Another cage with one mouse from each group was also prepared. A total of 5 mice from each treatment and the WT group were analyzed. Each IVC was positioned on a capacitive sensor board featuring

12 evenly spaced electrodes. The sensor board detected the presence of an animal by monitoring changes in capacitance across electrodes, primarily due to the animal's physiological composition (70% water) and movement. Subsequently, an Animal Locomotion Index (ALI) was calculated. This is based on the number of electrodes activated, with 0% = no electrodes and 100% = all 12 electrodes simultaneously activated within the time bin. The DVC Analytics platform provides real-time access to the data for visual inspection and download. The system default minimum activity binning was set to 1 min. Daily welfare evaluations were performed, with the cages being removed from the rack for animal inspection for less than 5 minutes.

Rotarod test

Motor learning was assessed using a mouse-accelerating RotaRod (Ugo Basile) as previously described.[95] Mice were placed on the rotating drum that accelerated from 5 to 40 rpm over 5 minutes. Mice were tested for three trials a day for two consecutive days, as shown in Figures 7E and 7F. The inter-trial interval was one hour. Rotarod scores were used to measure latency to fall or ride the rod for all three cohorts.

Open-field evaluations

The Open Field is the most used test for spontaneous exploratory activity in a novel environment, incorporating measurements of locomotion.[96] The Open Field test was performed following previously described protocols.[97] Exploration was monitored during a 60-minute session with Activity Monitor Version 7 tracking software (Med Associates, Inc.). Briefly, each mouse was gently placed in the center of a clear Plexiglas arena, measuring 27.31 x 27.31 x 20.32 cm (Med Associates, ENV-510), lit with dim light (approximately 5 lux), and allowed to ambulate freely. Infrared (IR) beams embedded along the arena's X, Y, and Z axes automatically track distance moved, horizontal movement, vertical movement, stereotypies, and time spent in the center zone. Data are analyzed in six 10-minute time bins. Arenas are cleaned with 70% ethanol and thoroughly dried between trials.

Catwalk

The murine free-pacing gait analysis was performed and evaluated using the Catwalk XT system (Noldus Information Technology), which consists of an illuminated walled glass walkway (130 cm x 10 cm) and a high-speed camera underneath, as previously described.[98] When downward pressure is applied, light is reflected, illuminating the stimulus (*i.e.,* the footprint). Walking patterns are captured with a high-speed camera mounted underneath the walkway. The experiment was done with dim room illumination (30 lux). The mouse can traverse the walkway as many times as needed to obtain at least three compliant runs (runs with a speed variation under 80% in 20 seconds or less). Pilot experiments using a 60% speed variation limit (most common in the literature) proved too stringent for most heterozygous mice. Parameters automatically collected by the software include but are not limited to paw statistics, intensity measures, stride length, width, the base of support, the distance between ipsilateral prints, cadence, % limb support, regularity index, speed, and speed variation. A highly trained experimenter visually inspected all automatically scored runs and manually classified any prints that were too ambiguous for the software to identify accurately.

Acoustic startle response

The acoustic startle response was tested using the SR-LAB Startle Response System with SR-LAB software (San Diego Instruments, San Diego, CA), as described previously.[99] Test sessions began by placing the mouse in the Plexiglas holding cylinder for a 5-minute acclimation period. For the next 8 min, mice were presented with each of six trial types across six discrete blocks of trials for 36 trials. The intertrial interval was 10–20 s. One trial type measured the response to no stimulus (baseline movement). The other five trial types measured startle responses to 40 ms sound bursts of 80, 90, 100, 110, or 120 dB. The six trial types were presented in pseudorandom order such that each trial type was presented once within a block of six trials. Startle amplitude was measured every 1 ms over a 65 ms period beginning at the onset of the startle stimulus. The maximum startle amplitude over this sampling period was taken as the dependent variable. A background noise level of 70 dB was maintained throughout the test session.

Survival analysis

The survival analysis was performed in a separate cohort of animals (n=10 and 16 mice/group). Lifespan was recorded as the age in days of each mouse on the date of death or euthanized due to humane endpoints when they became moribund. This late disease stage is defined as the point at which the mouse exhibits one of the following: complete limb paralysis and inability to move; >25% of maximal body weight lost; inability to eat or drink; lack of response to tactile stimuli. Mice were euthanized by carbon dioxide (CO_2) inhalation followed by cervical dislocation as per local IACUC protocol guidelines. Regarding animal numbers, 16 Twi mice/group (8M; 8F) were used. Survival analysis was performed using the Log-rank (Mantel-Cox) and Gehan-Breslow-Wilcoxon tests, with *p*-values of 0.0081 and 0.0044, respectively.

NMR experiments

For the screening of the CD derivatives that show stronger interactions with PSY, the ^{1}H-NMR samples contained 0.333 mL of buffer (0.2 M K_2HPO_4/0.2 M $KHPO_4$, pH not adjusted) in D_2O, 17.5 mL of CD_3OD, 50 mM of PSY, and 70 mM of CD analog. Spectra were recorded on an 800 MHz Bruker AVANCE III spectrometer equipped with a TCI-HCN cryoprobe. All the spectra were recorded at 300 K, and the temperature was calibrated to be the exact value of the sample space. To observe the relatively weak peaks from

PSY close to the HOD peak at 4.7 ppm, an excitation sculpting water suppression scheme was employed, as previously described.[100] The water suppression bandwidth was optimized to 250 Hz. For each spectrum, 360 scans were acquired with 64K points in the time domain for an effective acquisition time of 4.0 s per scan, with a recycle delay of 1 s. The total acquisition time for each sample was approximately 30 minutes. The time-domain data were Fourier transformed with a digital size of 128K after applying an exponential window with a 1 Hz line broadening factor. For the ^{1}H-NMR titration experiment, using the HPaCD (average DS: ~3.6, average MW: ~1180) as a titrant, a solution of PSY (1.0 mg) was dissolved in 1.0 mL of D_2O, achieving 2.2 mM concentration. The ^{1}H-NMR spectrum of this solution was recorded on a Bruker Advance 400 MHz NMR instrument. A titrant stock solution (6.6 mM) of HPaCD was then prepared by dissolving 7.8 mg of HPaCD in 0.1 mL of D_2O. Aliquots of the titrant solution were then added to the PSY solution. After each addition, the mixture was thoroughly mixed, and the ^{1}H-NMR spectrum of the mixture was recorded. Adding specific volumes of the titrant stock solution (6.6. mM), seventeen concentrations, ranging from 0.1 to 3.0 Eq of HPaCD, were prepared with the solution containing 2.2 mM of PSY (Figure 4).

LC-MS/MS

Cerebrum, spinal cord, and sciatic nerve specimens from C57/BL6 Twitcher mice (*Galc*$^{twi/twi}$) and age-matched C57BL6 *Galc*$^{wt/wt}$ (WT) were dissected and homogenized in 9:1 (v/v) in methanol containing 2 ng/mL of galactosyl(β) Sphingosine-d5 (AvantiResearch, #330714), which is a D_5-psychosine deuterated-labeled used as an internal standard (IDS) for quantitative MRM measurements.[24] A Liquid-Chromatography Tandem Mass Spectrometry (LC-MS/MS) PSY quantification was based on a previous method.[39] An Acquity UPLC HSS C18 (2.1x100mm, 1.8um; Waters #186003533) on a Waters Acquity UPLC system was coupled to Waters Xevo TQS for LC-MS/MS measurements. The flow rate is 0.3ml/min, and the temperature of the column is 40°C. The mobile phases comprised 0.1% Formic acid (mobile phase A) and acetonitrile containing 0.1% Formic acid (mobile phase B). The ESI (electrospray ionization) source was operated in positive ion mode at 3 KV. The desolvation temperature was kept at 50°C, and the desolvation gas flow was 1000L/h with cone gas at 150L/h. Multiple reaction monitoring (MRM) transitions were used to generate fragment ions from precursor [M+H]+ ions, which are 462.41>282.34(PSY) and 467.4>287.4(d5-PSY). For each LC-MS/MS run, a calibration curve was performed using standard PSY (galactosyl(β) Sphingosine; AvantiResearch, #330715), ranging from $2.56x10^{-5}$ to 10 ng/mL, diluted with the lipid extraction solution containing 2 ng/mL ISD. The calibration curve was used in MassLynx 4.1 software for data analysis. The dry weight of the specimens and the total body weight of the mice were used to standardize the PSY measurements for each specimen. Plasma, urine, and stool specimens collected from Twi and WT mice were extracted by homogenization in 9:1 (v/v) methanol containing 2 ng/mL d5-PSY (AvantiResearch, #330714). For all samples, after proper weighing, the specimens were placed in soft tissue homogenizing mix 2(OMNI#19-627)- or 7-mL(OMNI# 19-374) tubes, containing 1.4 mm ceramic beads. The BEAD RUPTOR 4 homogenizer (OMIN#SKU: 25-010) was used.

Urinary clearance of PSY

According to the principle of renal clearance outlined previously,[101,102] clearance is defined as the volume of plasma completely cleared of a substance per unit of time and is calculated as follows: $Cl = (U_{psy} \times V)/P_{psy.}$ C is the clearance (μL/min) for PSY in this case. U is the urine concentration of PSY. V is the urine flow rate (volume of urine per unit of time; here used as μL/min); P is the plasma concentration of the substance.

Neuropathology specimen preparation and assay allocation

Each animal treated with HPaCD and vehicle-only has its brain, spinal cord, and sciatic nerves harvested at PND 36-38. A total of 12 (six males and six females) were used per treatment cohort, which included the HPaCD and vehicle treatment mice. Before harvesting organs, mice underwent body perfusion preceded by anesthesia with isoflurane at 4-5% concentration using an induction chamber. After deep plan anesthesia was achieved, the mouse thoracic cage was opened, exposing the right ventricle, to which an incision was made with an iris scissor. Subsequently, a 25-gauge needle, connected to a peristaltic pump via silicon tubing, was inserted into the left ventricle. The perfusion was performed with cold PBS (~4°C) containing 10,000 units/L of heparin. The solution was infused continuously using a syringe pump at an infusion rate of 1.2-1.5 mL/h for 10 minutes, as previously described. No perfusion fixation solution was used as part of the samples harvested, as some of the specimens would undergo total lipid extraction for PSY measurements. Other specimens were used for immunohistochemistry assays and scanning electron microscopy (SEM). One cerebrum hemisphere was processed for immunohistochemistry assays and fixed by immersion in 4% paraformaldehyde (PFA) in phosphate-buffered saline (PBS; pH 7.4) for one day and processed in a sucrose gradient as previously described.[7] To determine PSY levels, the other brain hemisphere, one sciatic nerve, and half of the spinal cord segment were snap-frozen after dissection, and their dry weight was recorded for standardization of PSY measurements. These specimens underwent total lipid extraction using methanol with 2 ng/mL of D5-PSY standards. For the sciatic nerves, the contralateral sciatic nerve underwent fixation and preparation for scanning electron microscopy, as described below.

Brain sections and immunofluorescence staining

For the immunofluorescence, snap-frozen brain specimens were cryosectioned at 14-16 uM and mounted to regular Superfrost slides (Fisher). The immunofluorescence staining was performed using cold PFA 4% (~4 °C) in PBS for fixation for 20 minutes, followed by permeabilization with 0.1% Triton-X in phosphate saline (PBS) buffer, 60 minutes of blocking with 5% goat serum in PBS

before incubation with primary antibodies overnight.[7] The slides were washed three times with PBS before loading the secondary antibody for 4 hours. The slides were mounted with ProLong™ Gold (cat.# P36934). The following primary antibodies were used: rabbit anti-glial fibrillary acidic protein (GFAP; Encor, catalog#RPCA-GFAP), and goat anti-myelin basic protein (MBP; Encor, catalog# GPCA-MBP). The following secondary antibodies were used: F(ab')2 fragment AlexFluor 488 donkey anti-rabbit (Jackson Labs; cat.# 711-546-152); F(ab')2 fragment AlexFluor 594 donkey anti-goat (Jackson Labs; cat.# 705-586-147). Images were captured using the Cytation 5 imaging instrument (Agilent, Santa Clara, CA).

Electron microscopy and morphometric analysis

One of the dissected sciatic nerves from each mouse was incubated overnight in 4%PFA/2.5% glutaraldehyde in PBS and then transferred to sodium phosphate 10 mM containing 0.02% sodium azide for storage at 4°C until processing. After being postfixed, sciatic nerves were dissected and further treated for epoxy resin embedding as previously described.[59,103] Nerves were removed and postfixed in the same fixative for 2 hours at room temperature, then at least 72 hr at 4°C with gentle agitation. Samples were washed in 0.1 M sodium cacodylate and post-fixed for 2 hrs in 1% osmium tetroxide (Electron Microscopy Science, EMS, PA) in 0.1 M sodium cacodylate. Nerves were then dehydrated in increasing concentrations of ethanol followed by propylene oxide (PO, EMS), infiltrated with PO:EMbed 812 (EMS), and embedded in 100% EMbed 812 (EMS). Tissue blocks were sectioned on a Leica UC6 ultramicrotome (Leica, Wienna, Austria) at a thickness of 1 μm for semithin and stained with 1% toluidine blue to check the quality of the sample. 70 nm ultrathin sections were placed on 2 x 1 mm copper slotted formvar grids (EMS) and counterstained with 3% uranyl acetate in 50% methanol for 20 min, followed by lead citrate for 5 min. Large tilescans of entire nerve cross sections were acquired using a Zeiss Gemini300 FESEM (Carl Zeiss Microscopy, Oberkochen, Germany) in STEM mode with acceleration at a voltage of 20kV. For the morphometric analysis, AxonDeepSeg, developed at the NeuroPoly Lab, Polytechnique Montreal, University of Montreal, Canada, is an open-source software that utilizes deep learning to segment axons and myelin sheaths from microscopy images automatically.[58] Using the TEM images captured, the G-ratio parameters, including the inner axon diameter to the outer diameter of the myelinated fiber, were measured in individual myelinated axons and calculated as previously described.[70] This is the only axon morphometric parameter that was not calculated using the AxonDeepSeg analysis software.

TNFα ELISA

Sciatic nerve lysates were harvested and processed using RIPA buffer. TNFα levels were measured using the TNFα Human High Sensitivity ELISA (BMS223HS; Invitrogen, Thermo Fisher Scientific, Waltham, MA, USA). The total protein content in cell lysates was quantified using the bicinchoninic acid assay (BCA). Cell cytokine release was expressed in pg of TNFα/mg of protein.

QUANTIFICATION AND STATISTICAL ANALYSIS

Statistical analyses were performed with GraphPad Prism v10.4.1(532) (GraphPad Software, LLC). Multiple comparisons were performed to assess statistical significance. When uniform variance of the results was identified by Bartlett's analysis ($p<0.05$), one-way analysis of variance (ANOVA) was used to test for statistically significant differences. When significant differences ($p < 0.05$) were identified, the results were further analyzed by Dunnett's or the Tukey–Kramer multiple range test to determine the significance of differences between the groups. Where uniform variance of the results was not identified, non-parametric multiple comparisons were performed—after confirming significant differences ($p<0.05$) using Kruskal-Wallis analysis, the differences were examined by applying Dunn's multiple comparison test. Two-way ANOVA was performed to evaluate statistical significance. When significant differences ($p < 0.05$) were identified, the data were further analyzed using Dunnett's multiple comparison test. Figure legends indicate sample sizes, and significance was defined as p-value*<0.05, p**<0.01, p***<0.001, p****<0.0001, ns: non-significant.

Regarding rigor and reproducibility, the number of replicates and statistical analyses were reported in the figure and table legends, supplementary information, and source data files. All comparisons were planned in advance of each experiment, based on previously published studies. Statistical methods were used for power analyses to estimate the number of animal subjects required for *in vivo* experiments. Based on previous studies, the murine cohort size calculations were used to determine the number of subjects required for α=0.05 and β=0.9, variability of the endpoint examinations (*e.g.,* PSY levels, neurobehavioral assessments, etc), and specific inferential statistical analyses. Outlier data were not excluded from the analysis. For the neurobehavioral evaluations, mice that did not complete the treatment for different reasons were excluded from the analysis and results presented. The data were replicated using technical and biological replicates, with a minimum of three. The figure legends and supplementary information contain the information. The researchers who performed *in vivo* studies, including drug/vehicle administration, were blinded to the cohort assignment.